U.S. Department of Energy
Energy Efficiency and Renewable Energy
Vehicle Technologies Program
Award: DE-EE0006082

FINAL TECHNICAL REPORT

Computational Design and Development of a New, Lightweight Cast Alloy for Advanced Cylinder Heads in High-Efficiency, Light-duty Engines

Principal Investigator: Mike J. Walker
mike.j.walker@gm.com
(586) 651-3757

Principal Investigator: Qigui Wang
Qigui.wang@gm.com
(248) 762 6332

Recipient: General Motors LLC
30500 Mound Rd, Mail Code 480-106-300
Warren MI 48092-2031

Subrecipients/Partners: QuesTek Innovations LLC, Northwestern University, American Foundry Society, Camanoe Associates, Fred Major, Secat Inc.

Period of Performance 02/01/2013 through 06/30/2018

Date of Submission: September 28, 2018

Contents

1. Executive Summary

The objective of the collaborative multi-year Cast Lightweight Alloy program summarized in this report is to develop a new, lightweight, cast aluminum alloy for automotive engines with better high temperature properties than the incumbent alloys (B319, A356, A356+0.5Cu) to allow for more efficient engine operation. The current alloys show a sharp decrease in strength at high temperatures (200-300˚C) limiting the operating temperature of the engine. The high strength in cast aluminum alloys is usually achieved by precipitation hardening (using θ'-phase or β'-phase), but the strengthening potency of the precipitates decreases at higher temperature due to excessive coarsening or dissolution of the precipitate. Hence, to design an alloy that maintains strength at high temperatures, a coarsening- and dissolution-resistant precipitate needs to be developed. Figure 1 outlines the overall system design chart for the design problem highlighting the focus of the current program (Solution treatment/ Aging → Strengthening dispersion → Tensile/ Fatigue Strength at high temperatures).

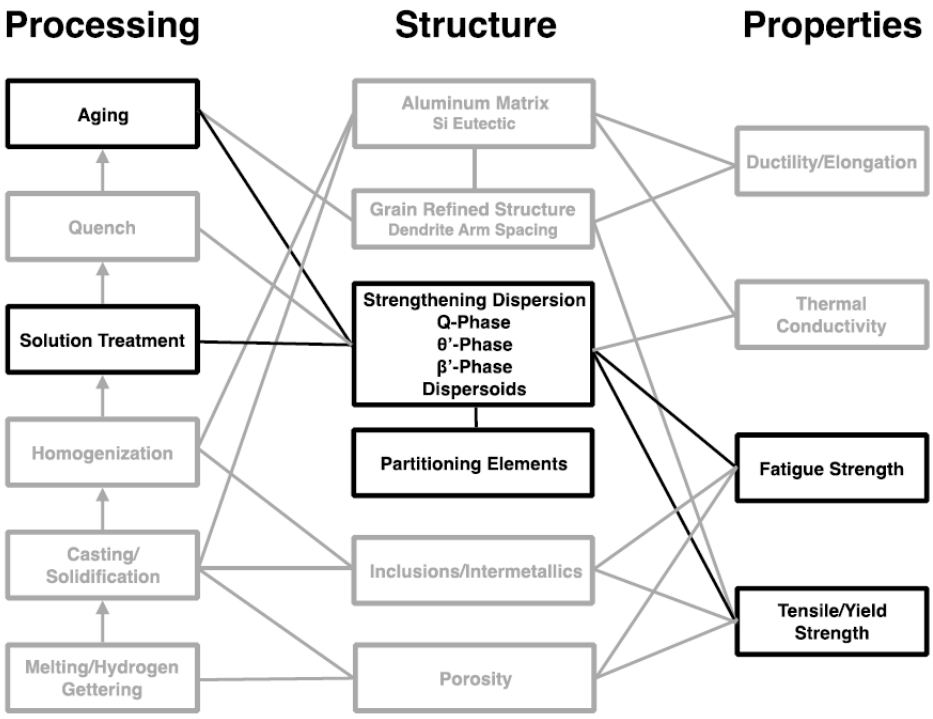

Figure 1. System design chart for design of high-temperature Al alloy

The program kicked off with the generation of alloy concepts and selecting alloy models (Task 2.0) with specific milestones for establishing property requirements (Milestone 1), generating design concepts (Milestone 2) and selecting models for casting design (Milestone 3). Details about the design concepts and computational models are discussed in *Section 3 – Overview of design concepts* and *Section 5 - Modeling Approach* respectively. Following this, sub-scale prototypes of the promising design concepts were cast and characterized (Task 3.0) in order to validate the design concepts and develop data for subsequent model calibration and improvement. Using the calibrated models, a set of alloy designs were created (Task 4.0) which are summarized in the Milestone 7 report. This first generation set of designs were validated (Task

5.0) through production and characterization of lab-scale castings (Milestones 8 and 9). With the learnings from the lab-scale prototypes and the improvements in the computational models, final embodiment design of the new alloy was completed as part of Task 6.0 (Milestone 10). The final alloy designs were cast at lab-scale (Milestone 11) and also at component-scale (Milestone 12) to characterize its final properties (Milestone 14). Properties of the final castings are described in *Section 2 – Comparison of Developed Cast Alloy properties to DOE Targets*.

An alloy recyclability analysis was performed (Task 8.0/Milestone 13) and is summarized in Section 7 Recyclability Analysis.

Cost modeling was performed in Phase 2 of the project, in which Tasks 10.0 and 11.0 were focused on development of alloy and component production cost models, respectively. The results of the cost modeling development effort was summarized in Milestone 15 and is summarized in Section 8 Cost Analysis.

2. Comparison of Developed Cast Alloy properties to DOE Targets

Department of Energy targets for the Cast Lightweight Alloy Project are shown in Table 1. A comparison of these targets is made to a common production alloy Alloy 1 and to the newly developed strengthened Q-phase alloys. This program carried out two cylinder head casting trials and the alloys chemistries and designations are identified in Table 2. Alloy 1 is basically A356.1 alloy with 0.5 wt% Cu added. Alloy 2 Trial 1 increases the amount of Q-phase by adding additional Cu and Mg. It also adds Si and Ni which has been shown to increase higher temperature properties and also adds Zr and V that have been shown to segregate to and stabilize the Q-phase. Alloy 1 is used again in Trial 2 as the baseline comparison. Alloy 2 Trial 2 again increases the Cu and Mg contents to increase the amount of Q-phase and adds the Q-phase stabilizing elements Zr and V. However because of the low ductility seen in Alloy 2 of Trial 1, Si was not increased and Ni was also not added.

Table 3 material property comparisons to DOE targets were based on combustion chamber and deckface samples of cylinder head castings. These regions were chosen for this comparison because these are the most critical areas of the head for ductility and high temperature properties. These regions are cast next to water cooled steel tooling for the lowest secondary dendrite arm spacing (SDAS) and the highest ductility. Tensile property measurements made above 200°C were only performed in the combustion chamber and deckface regions because it is only in these locations such temperatures exist in an engine. Samples were also extracted from other regions such as high pressure oil galleries and head bolt bosses. These regions are isolated from the chilled surfaces and are surrounded by sand cores. In these regions, SDAS is larger, porosity is typically greater and ductility is also typically lower. Material property comparisons to targets in these slower cooled regions will also be highlighted. Material tensile strength and fatigue properties measured above 150°C were first pre-conditioned at the test temperature for 100 hours. Pre-conditioning coarsens precipitate structures and lowers material properties.

Table 1. DOE Baseline and Targets of Cast Lightweight Alloy

Property	Cast Aluminum Baseline	Cast Lightweight Alloy Targets	Key Properties (must meet)
Tensile Strength (Ksi)	33 KSI	40 KSI	Key
Yield Strength (Ksi)	24 KSI	30 KSI	Key
Density	2.7 g/cm^3	< 6.4 g/cm^3	Key
Elongation (%)	3.5 %	3.5 %	
Shear Strength	26 KSI	30 KSI	
Endurance Limit	8.5 KSI	11 KSI	
Fluidity (Die Filling Capacity/Spiral Test)	Excellent	Excellent	Key
Hot Tearing Resistance	Excellent	Excellent	Key
High Temperature Performance	@ 250C	@ 300 C	
Tensile Strength (KSI)	7.5KSI @ 250 C	9.5 KSI @ 300 C	Key
Yield Strength (KSI)	5 KSI @ 250 C	6.5 KSI @ 300 C	Key
Elongation in 2"	20% @ 250 C	< 20% @ 300 C	

Table 2. Chemistry of alloys used in engine cylinder head trials

	Si	Cu	Mg	Ni	Zr	V	Fe	Sr	Al
Alloy 1	6.5-7.5	0.4-0.6	0.25-0.45	0.05 max	n/a	n/a	0.15 max	0.005-0.02	rem
Alloy 2 Trial 1	7.5-8.5	0.7-0.8	0.35-0.45	0.1-0.15	0.1-0.15	0.1-0.15	0.15 max	0.005-0.02	rem
Alloy 2 Trial 2	6.5-7.5	0.7-0.8	0.35-0.45	0.05-0.1	0.1-0.15	0.1-0.15	0.15 max	0.05-0.02	rem

Table 3. A comparison of measured alloy properties to DOE targets for a common production alloy (Alloy 1), and for the strengthened Q-phase alloys (Alloy 2 Trial 1 and Alloy 2 Trial 2)

Property	DOE Cast Lightweight Alloy Target	Alloy 1 Trial 1/2		Alloy 2 Trial 1	Alloy 2 Trial 2
Tensile Strength @RT (MPa)	276	313	311	323	321
Yield Strength @RT (MPa)	207	251	260	275	265
Density (g/cc)	<6.4	2.7		2.7	2.7
Elongation (%)	3.5	6.2	6.1	2.3	4.5
Fatigue Strength 10^7 Cycles	75	65	80	90	69
Fatigue Strength 10^4 Cycles (MPa)	No Target	N/A	218	N/A	228
Castability (Fluidity and Hot Tearing Resistance)	Excellent	Excellent		Excellent	Excellent
Tensile Strength@300ºC, 100 hours	65	42	42	56	52
Yield Strength @ 300ºC, 100 hours	45	40	40	49	45
Elongation @ 300 ºC, 100 hours	<20%	28/44		9	37%

2.1 Tensile Properties

A plot of Alloy 2 Trial 2 tensile properties in the combustion chamber and deckface regions with a comparison to the targets are shown in Figure 2. At room temperature, both alloys were able to achieve the DOE targets. Q-phase based alloys (Alloys 1 and 2) provide room temperature strengths well above those of an A356 alloy. The ductility of Q-phase based alloys is better than the Theta-Q alloys such as B319 achieving the room temperature DOE ductility target. The increase in intermetallics by the addition of additional copper and the minor elements in Alloy 2 did result in slightly lower ductility compared to the Alloy 1.

At 300ºC, the strengthened Q-phase alloy did achieve the yield strength target while the production alloy did not. Neither alloy was able to achieve the ultimate strength targets or a total elongation target of less than 20 %. With regards to both the total elongation and UTS targets at 300ºC, any significant yielding of the material will result in engine distortion and would be unacceptable. As the greatest stresses and temperatures are in the bridge areas between valves, head distortion could lead to valve seat distortion resulting in poor valve seating, loss of compression, lower power, and higher emissions.

Of greater concern is the lack of improvement of strength properties in the mid temperature range 200°C and 250ºC. Although the minor elements, zirconium and vanadium have stabilized the Q-phase and produced an increase in tensile strength at 300°C, property differences at these midrange temperatures are insignificant. As will be shown in a later section, the minor elements reduce the growth of the Q-phase and increase the temperature of the coherent-incoherent transition, but these effects are not significant until the higher temperatures.

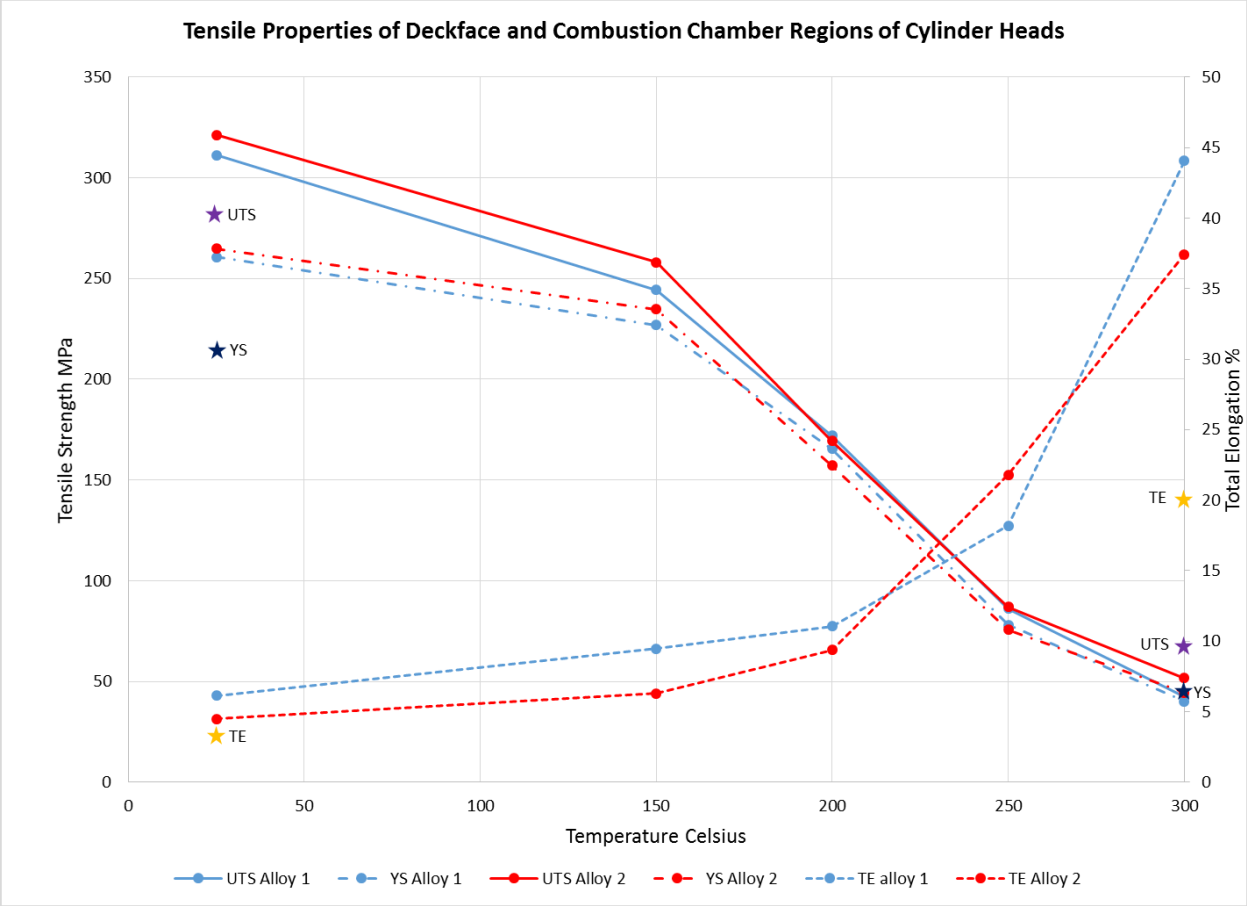

Figure 2. Tensile properties of a baseline 356 0.5%Cu alloy (Alloy 1) and developed alloy (Alloy 2 Trial 2) with comparison to DOE targets identified by colored stars. Tensile specimens were extracted from the deckface and combustion chambers and samples tested above 150°C were conditioned for 100 hours at test temperature before tensile testing.

Tensile properties for the bolt boss and high pressure oil line regions from room temperature to 200°C are shown in Figure 3 and Figure 5. High pressure oil lines are surrounded by sand and have poor directional solidification from the deckface to the risers. This results in greater porosity and larger intermetallic structures that are detrimental to the ductility. Fracture analysis was carried out on the high pressure oil line samples to determine the main cause of failure.

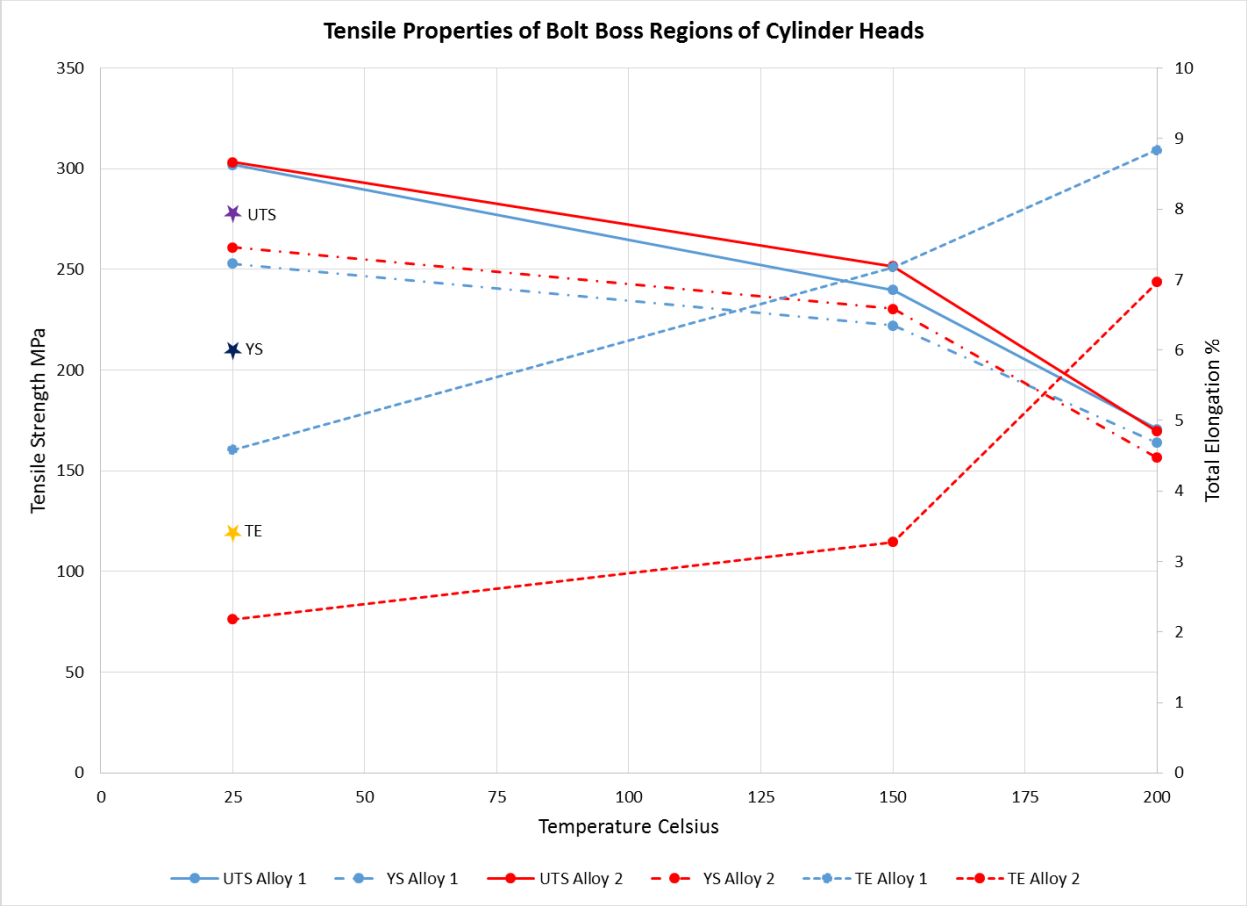

Figure 3. Tensile properties of a baseline 356 0.5%Cu alloy (Alloy 1) and developed alloy (Alloy 2 Trial 2) with comparison to DOE targets identified by colored stars. Tensile specimens were extracted from the bolt boss regions. Samples tested at 200°C were conditioned for 100 hours at test temperature before testing.

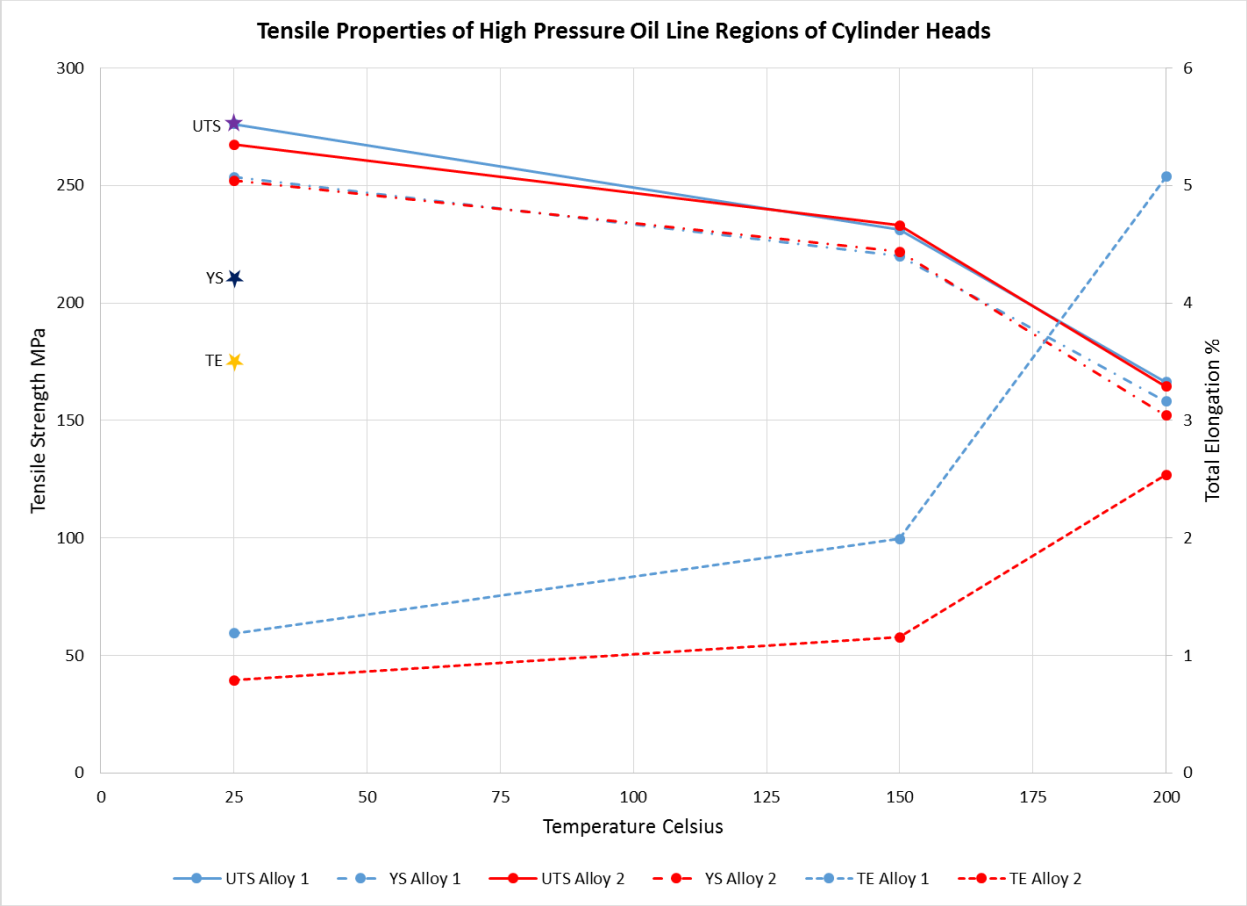

Figure 4. Tensile properties of a baseline 356 0.5%Cu alloy (Alloy 1) and developed alloy (Alloy 2) with comparison to DOE targets identified by colored stars. Tensile specimens were extracted from the high pressure oil line regions. Samples tested at 200ºC were conditioned for 100 hours at test temperature before testing.

2.2 Elastic Modulus

The elastic modulus was measured for each of the tensile specimens. All samples at each temperature were averaged together. The results are shown in Table 4. Samples tested above 150ºC were all conditioned for 100 hours at temperature. Results are similar to 356 and 356+0.5Cu.

Table 4. Measured elastic modulus of Alloy 2 specimens. Samples tested above 150ºC were all conditioned for 100 hours at temperature.

Temperature ºC	Average Elastic Modulus (GPa)	Number of samples
25	72	26
150	62	26
200	55	26
250	37	9
300	27	9

2.3 Fracture analysis of high pressure oil line tensile specimens

The high pressure oil lines were selected for fracture analysis because both the baseline alloy, Alloy 1 Trial 2, and the newly developed alloy, Alloy 2 Trial 2, showed very poor ductility at room temperature. Furthermore ultimate tensile strengths dropped significantly compared to both the bolt boss and the deckface specimens. Yield strengths were comparable which suggests that the ultimate tensile strengths were limited by significant defects which led to premature failure.

The reduced ductility can be attributed to two aspects in the material for a giving heat treatment condition. One is the increased volume fraction of intermetallic phases as observed in the first casting trail study. The other reason is the porosity. Porosity is commonly known as the most important factor affecting the tensile ductility of cast aluminum alloys. Pores are stress risers and act as crack initiators. Along with other cracked Si intermetallic particles, porosity provides weak paths for crack propagation. In general, the area fraction of porosity observed on the fracture surfaces can be more than 10 times higher than the volumetric fraction of porosity in the bulk material, indicating that the porosity is the weak link for crack initiation and propagation. Figure 5 shows fractographic images of tensile fracture surfaces of Alloy 1 and Alloy 2. There are notable pores on the fracture surfaces in both alloys although the overall fracture surface appears quasi-ductile in nature. Figure 6 shows the relationships between ductility and the area fraction of porosity observed on the fracture surfaces of the tensile samples of three alloys. In general, ductility decreases with the increase of porosity observed on the fracture surfaces particularly for the baseline alloy (Alloy 1). For Alloy 2, it appears that the increased volume fraction of intermetallic phases has notably reduced the sensitivity of ductility with porosity.

The size and volume fraction of porosity in aluminum castings is strongly related to alloy composition, melt treatment and particularly casting process. For a given casting process and melting practice, small variation of alloying elements can play a role in porosity as they affect castability of the material including freezing range, fluidity, feeding capability, hot tearing, etc. In our trial #2 casting study, however, the overall porosity observed in the high-pressure oil line (HPOL) tensile samples between the Alloy 1 and the Alloy 2 is very comparable partly due to the very small alloy composition change and partly due to the limitation of the current head casting process and sampling location. In the HPOL tensile samples tested and characterized, the average area fraction and one standard deviation of porosity observed on the fracture surfaces is 3.43%±1.83% and 3.75%±1.3% for Alloy 1 and the Alloy 2, respectively. Similar observations are also made in pore sizes in the HPOL tensile samples for both alloys. As shown in Figure 7 - Figure 9, the average pore size is 326 μm and 322 μm for the Alloy 1 and the Alloy 2, respectively.

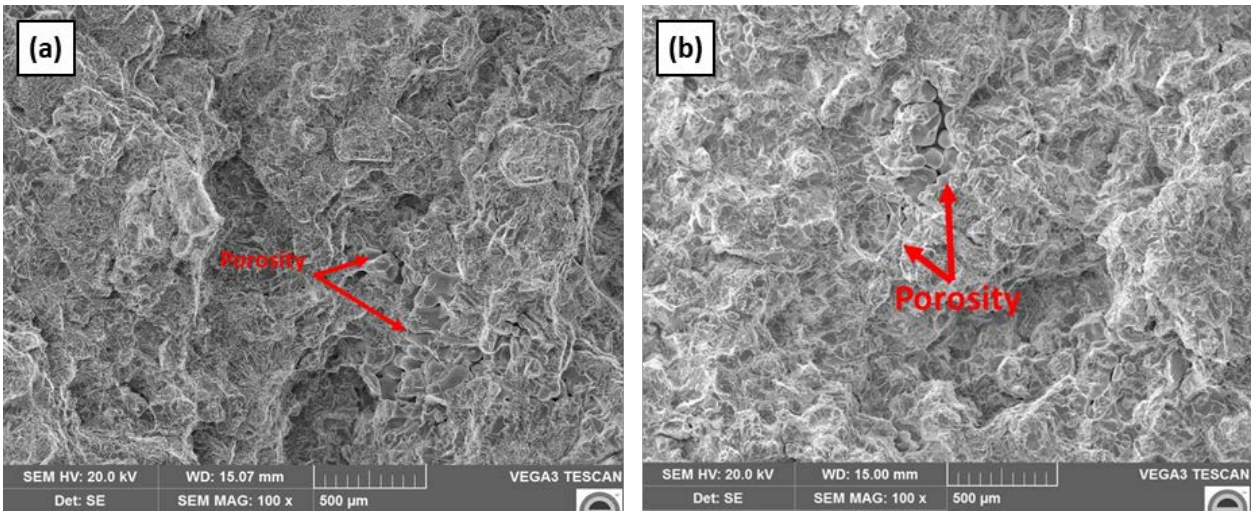

Figure 5. Fractographic images of (a) baseline alloy (Alloy 1 Trial 2) and (b) the newly developed alloy (Alloy 2 Trial 2).

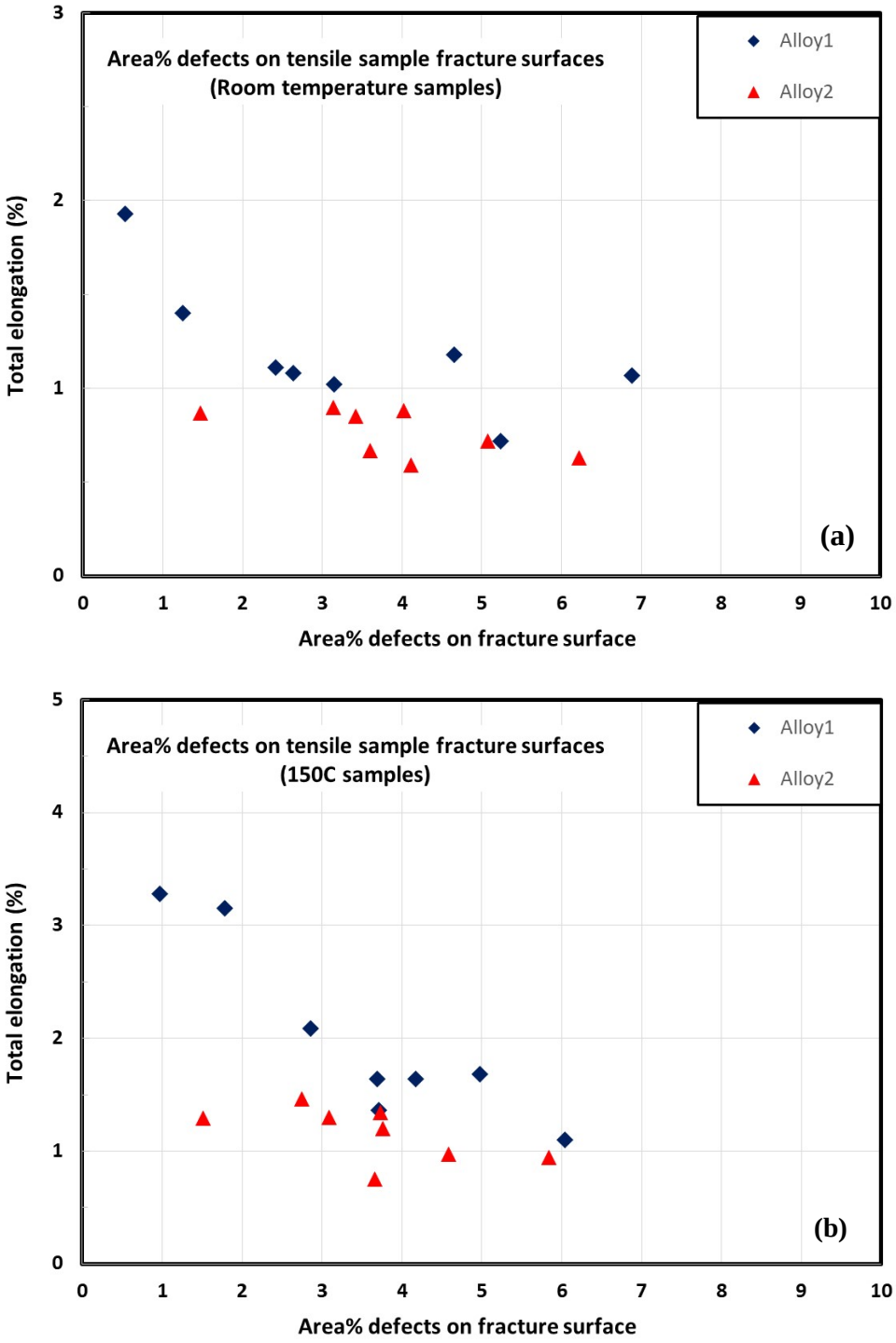

Figure 6. Relationship between tensile ductility (total elongation) and area fraction of porosity on the tensile fracture surfaces of two alloys (a) room temperature samples and (b) 150°C tensile samples.

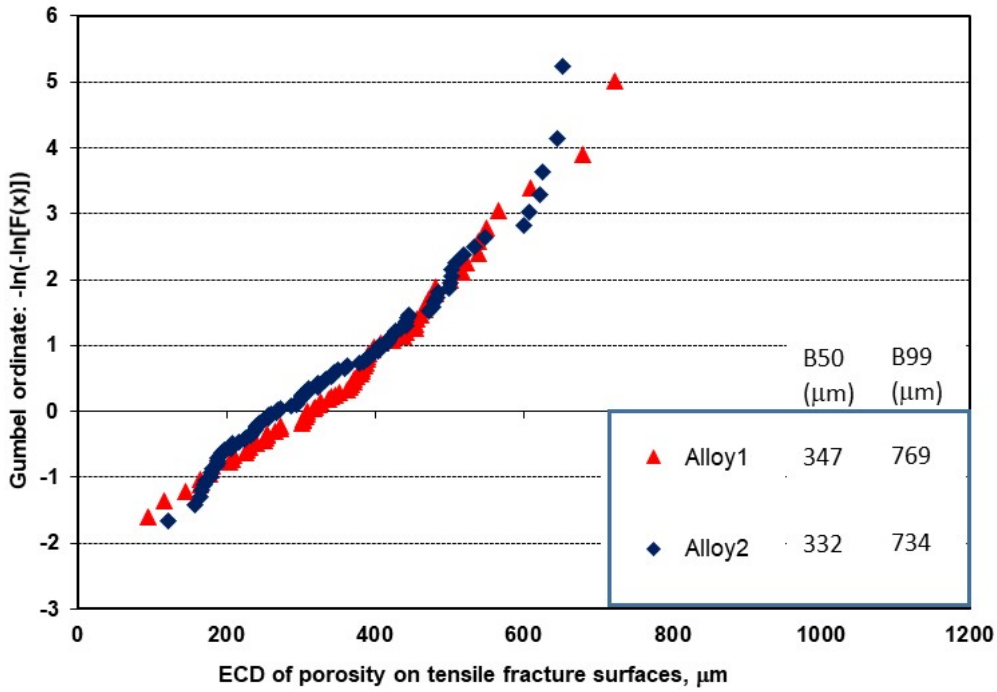

Figure 7. A comparison of defect sizes observed in the tensile fracture surfaces of samples taken from high pressure oil line locations of engine heads made of both Alloy 1 Trial 2and Alloy 2 Trial 2 and tested at room temperature.

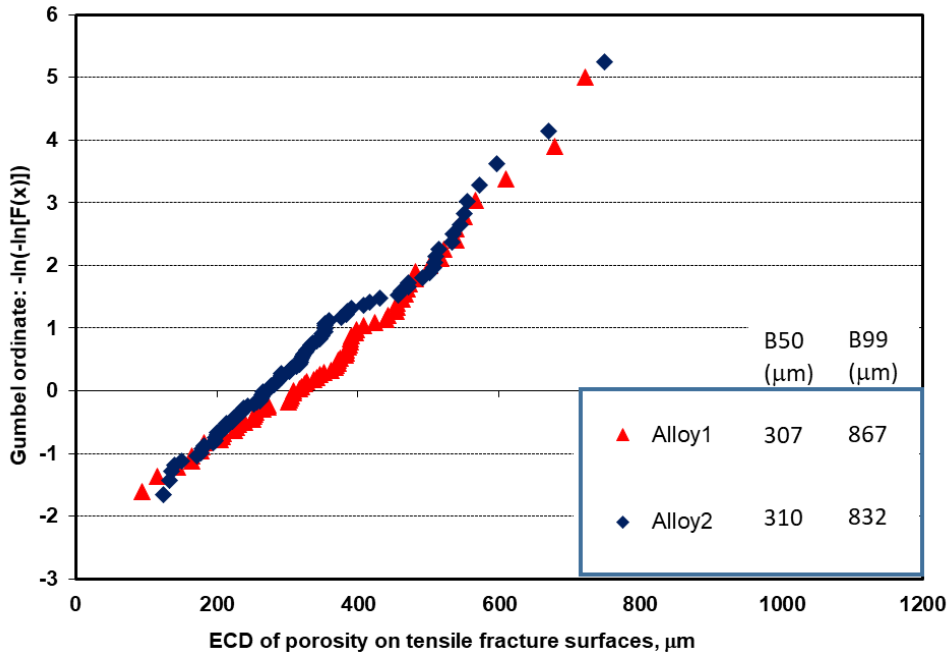

Figure 8. A comparison of defect sizes observed in the tensile fracture surfaces of samples taken from high pressure oil line locations of engine heads made of both Alloy 1 Trial 2and Alloy 2 Trial 2and tested at 150°C.

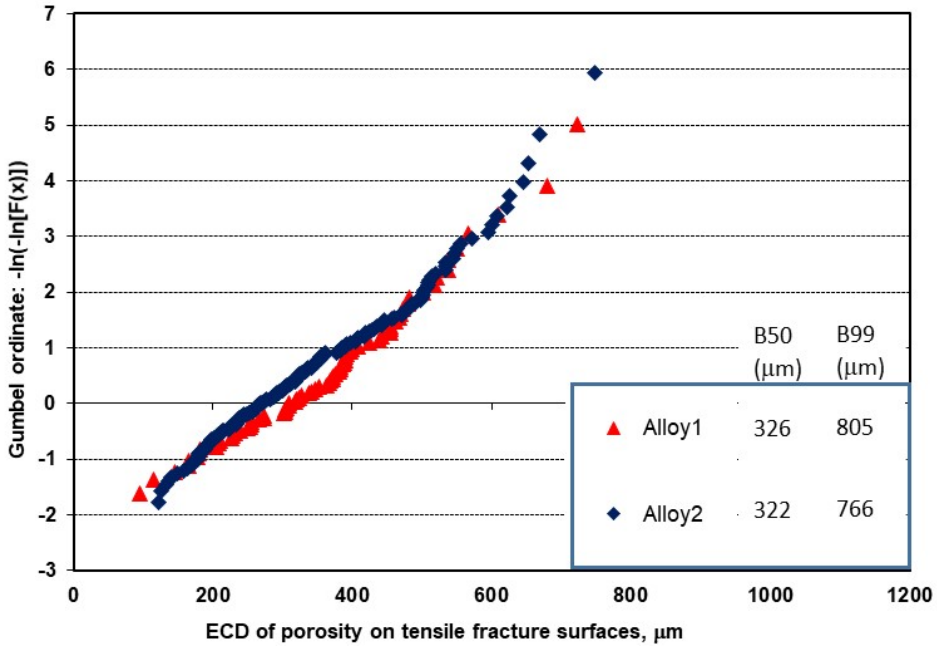

Figure 9. A comparison of defect sizes observed in the tensile fracture surfaces of samples taken from high pressure oil line locations of engine heads made of both Alloy 1 Trial 2and Alloy 2 Trial 2.

2.4 High Cycle Fatigue Strength

Table 3 it was shown that the high cycle fatigue strength (HCF) of the newly developed alloy Alloy 2 Trial 1 exceeded the DOE target of 75 MPa, however, Alloy 2 Trial 2 did not achieve the target. It must be recognized that fatigue results are subject to consider variability from one test to another. Furthermore, because HCF is controlled by defects such as porosity or oxides in aluminum alloys, the HCF strength is determined more by the casting process, hydrogen degassing, and metal cleanliness than the alloy composition. Table 5 shows the measured high cycle fatigue strength measured in three alloys in two casting trials. Beginning with Trial 1, Alloy 2 Trial 1 showed very promising HCF results in the deckface, combustion chamber, and bolt boss regions compared to the baseline alloy. However, the addition of the alloying components will increase eutectic silicon, Q-phase precipitates, and other intermetallics. The tensile strengths of Alloy 2 Trial 1 are not significantly improved over the baseline alloy and the ductility of these alloys are worse than the baseline. Therefore the HCF strength should not be improved based on the alloying additions and is more likely based on improved degassing or a change in the oxide distribution. For the second head casting trial, in the combustion region, Alloy 2 Trial 2 properties were worse than Alloy 1 Trial 2. However in the bolt boss and high pressure oil line regions, Alloy 2 Trial 2 properties were now better than Alloy 1 Trial 2 and for the bolt boss regions nearly met the DOE target. In summary, what can be concluded is that the HCF strength of the developed alloys are not significantly different than the baseline alloy. High cycle fatigue and low cycle fatigue strengths are the most critical material properties for cylinder head design. Unless a significant improvement in these properties can be shown in a new alloy or process, changes to the current bill of process or bill of materials will not be made. Further research is needed to improve the casting processes to produce engine cylinder heads before improved high temperature properties of the alloys can be utilized.

Table 5. High cycle strength (10^7 cycles) of cylinder head casting samples from two casting trials.

Region	Test Temperature (°C)	High Cycle Fatigue Strength (MPa)			
		Trial 1		Trial 2	
		Alloy 1	Alloy 2	Alloy 1	Alloy 2
Deckface and combustion chamber	25	65.5	90.3	80.4	69.4
	150	63.6	76.2	78.5	56.5
	200	62.3	N/A	57.0	75.6
	250	48.7	52.7	48.9	47.1
Bolt boss	25	N/A	N/A	73.7	73.7
	150	64.2	85.0	65.0	70.0
	200	N/A	N/A	62.5	63.7
	250	45.8	52.5	N/A	N/A
High pressure oil line	25	71.2	70.5	43.5	60.2
	150	64.5	68.0	47.2	51.8
	200	N/A	N/A	46.7	40.7
	250	44.5	47.2	N/A	N/A

2.5 Fracture analysis of high cycle fatigue samples for Trial 2

Fracture analysis of the fatigue samples for the second casting trial has been carried out. In general, the fatigue failure was caused by defects (porosity) in the samples. Figure 10 shows an example of a shrinkage-dominated pore that initiated the fatigue crack.

In deckface and combustion chamber areas, the HCF strengths of Alloy 1 are slightly better than those of Alloy 2 except for the 200°C samples. This can be well explained from the measured sizes of defects (porosity and oxides) that initiate fatigue cracks in the fatigue failure samples. As shown in Figure 11, the average (B50) defect size is 137μm in Alloy 1 and 152μm in Alloy 2. For the 200ºC samples, more samples were failed by large slip planes in the Alloy 1 although the average defect size in Alloy 1 is slightly smaller than that of Alloy 2. Figure 12 shows the large slip plane initiating the fatigue crack in one of the Alloy 1 samples.

In bolt boss locations, the fatigue strengths are quite comparable between two alloys at all three temperatures tested. As expected, the average (B50) sizes of defects that initiated fatigue cracks are also very comparable (216μm for Alloy 1 and 220μm for Alloy 2, Figure 13). Interestingly, it is noted that the scatter of defect sizes in Alloy 1 is larger than Alloy 2, which is similar to the results seen in deckface & combustion chamber locations.

In high pressure oil line (HPOL) areas, the fatigue strengths of Alloy 1 are generally lower than those of Alloy 2 at both room temperature and 150ºC. At 200ºC, however, the fatigue strength of Alloy 1 is higher than that of Alloy 2. Figure 14 compares the defect sizes in all HPOL samples between both alloys. It is interesting to note that the defect sizes in the Alloy 1 are generally smaller than those in the Alloy 2 (B50: 355μm for the Alloy 1 and 424μm for the Alloy 2), which cannot really explain the lower fatigue strengths tested in the Alloy 1 at both room temperature and 150C. Based on the fractographic observations, it was found that many HPOL samples in the Alloy 1 failed by large shear planes together with some small pores, as shown in Figure 15. After including the shear planes in the crack initiators, Figure 16, the new "defect" sizes in the Alloy 1 are larger than those in the Alloy 2 (B50: 559μm for the Alloy 1 and 424μm for the

Alloy 2). This indicates that large shear planes, probably due to columnar grain structure, can significantly reduce fatigue properties even though the defect sizes are small.

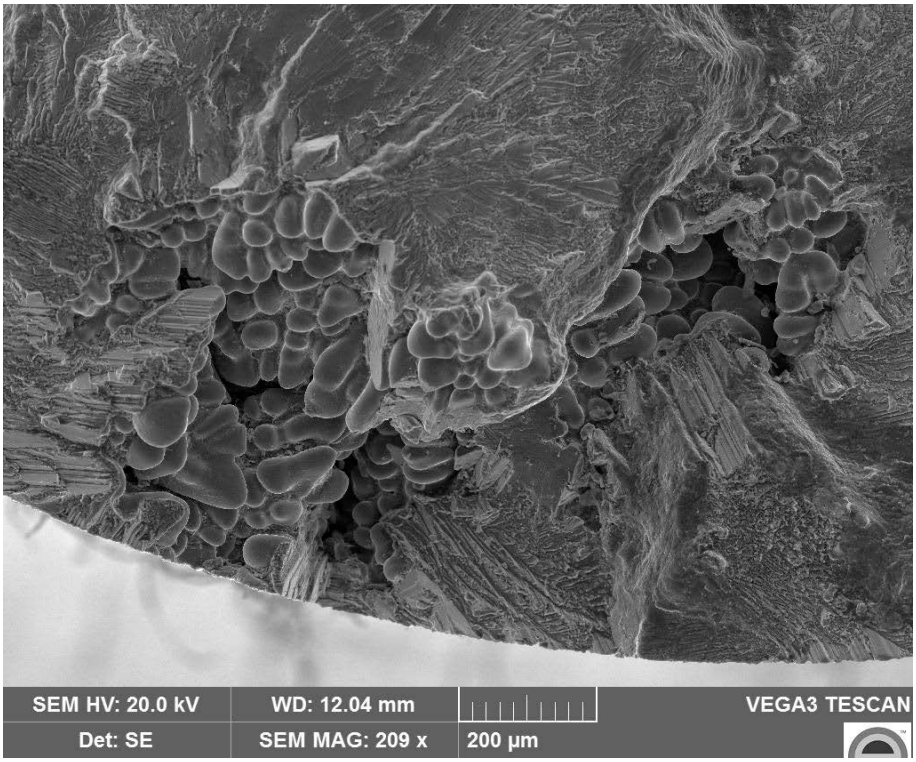

Figure 10. SEM image showing a shrinkage-dominated pore that initiated fatigue crack and significantly reduce the fatigue life in an Alloy 1 deckface sample (740971 cycles at 74MPa, ECD of pore: 687µm)

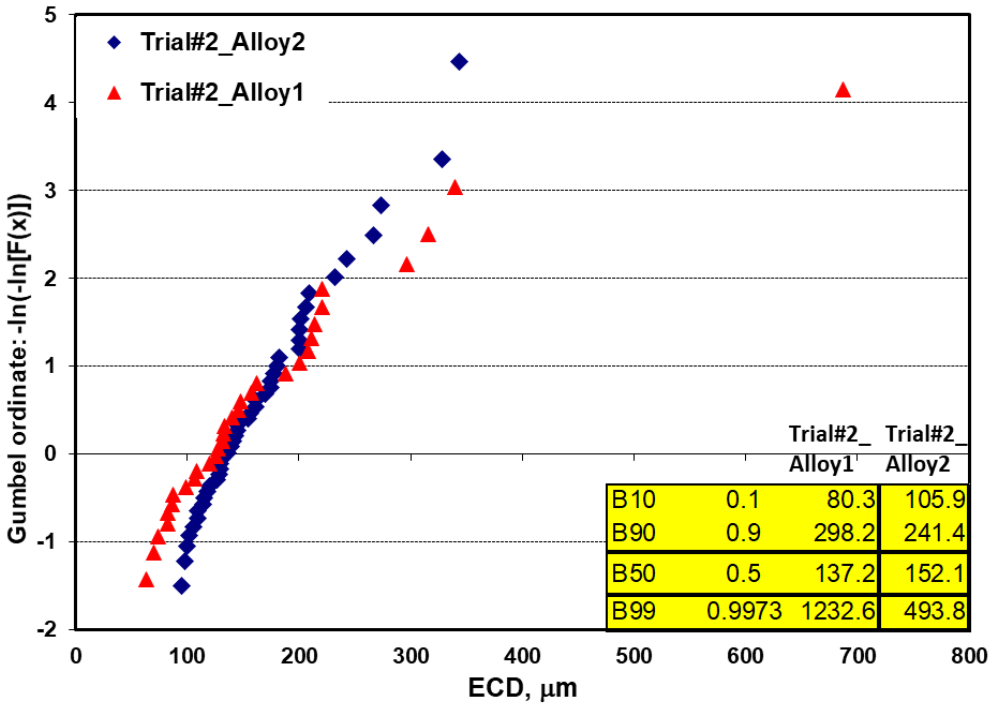

Figure 11. A comparison of size distributions of defects that initiated fatigue cracks in the deckface and combustion chamber areas of engine heads made of both Alloy 1 and Alloy 2.

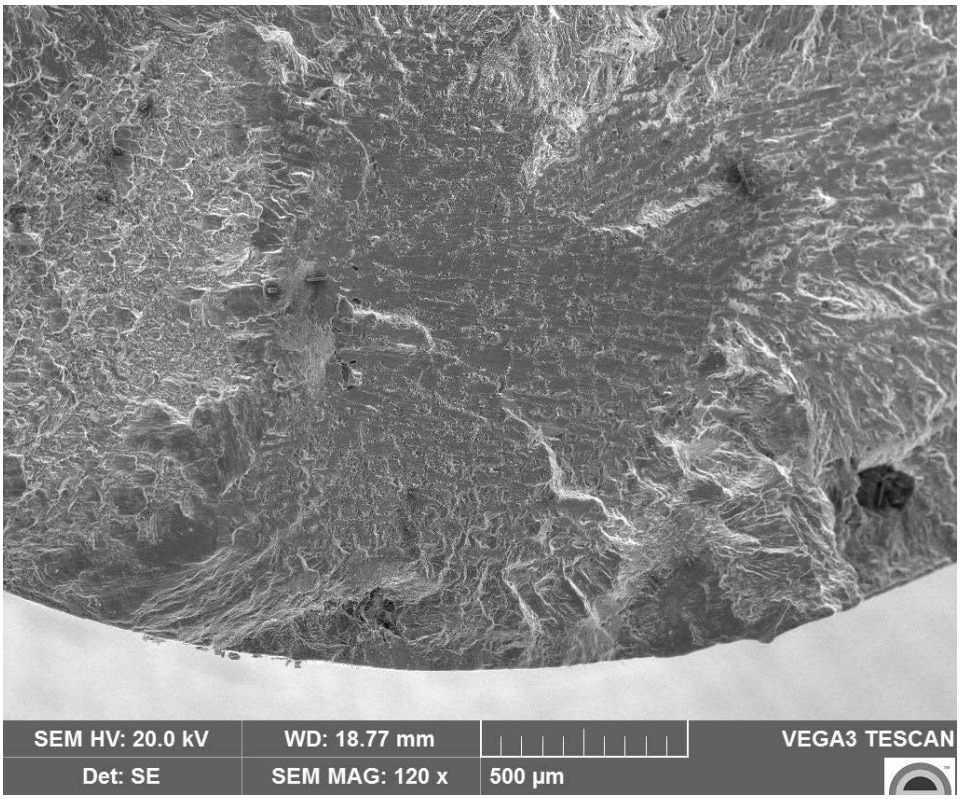

Figure 12. SEM image showing a large slip plane that initiated fatigue crack in a deckface sample of Alloy 1.

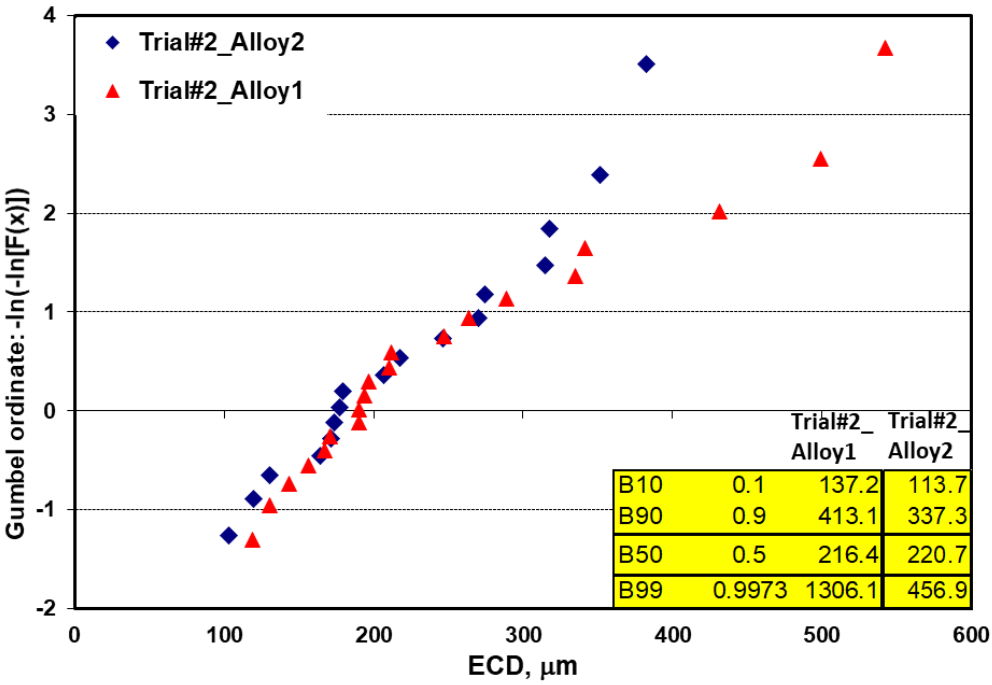

Figure 13. A comparison of size distributions of defects that initiated fatigue cracks in the bolt boss areas of engine heads made of both Alloy 1 and Alloy 2.

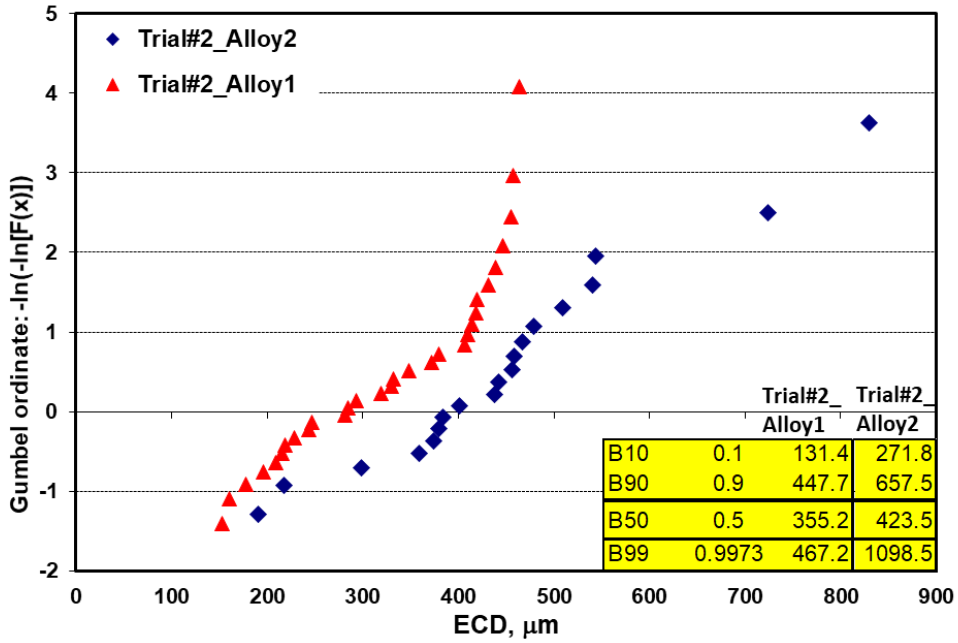

Figure 14. A comparison of size distributions of defects that initiated fatigue cracks in the high-pressure oil line locations of engine heads made of both Alloy 1 and Alloy 2.

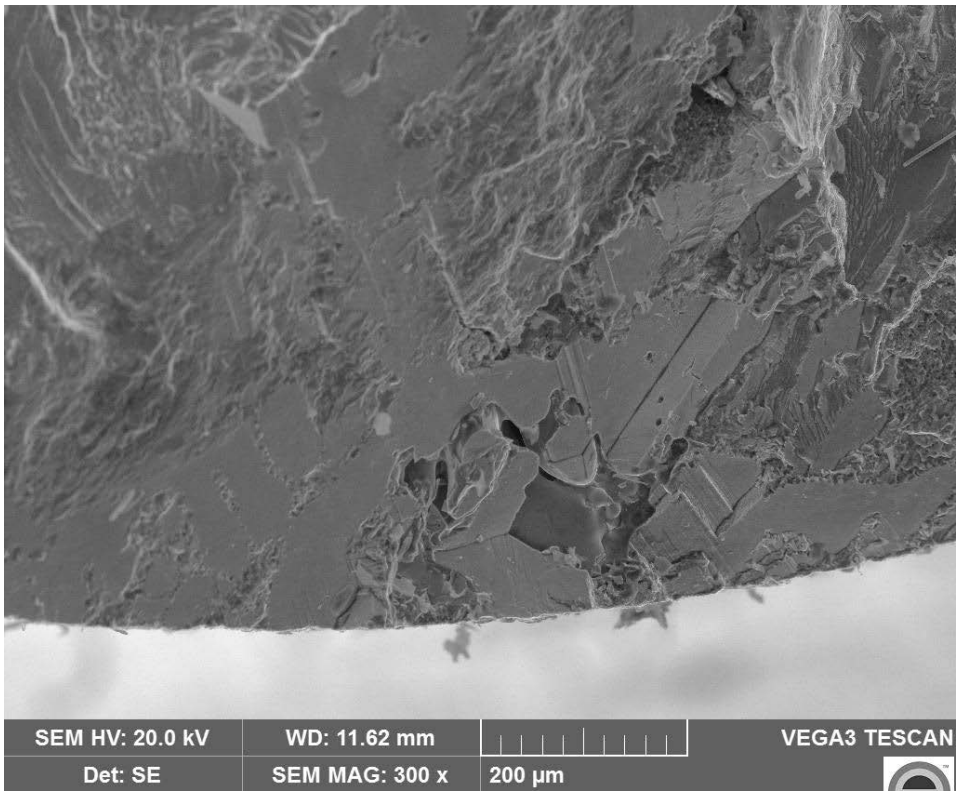

Figure 15. SEM image showing a large slip plane together with porosity that initiated fatigue crack in a high-pressure oil line (HPOL) samples of Alloy 1.

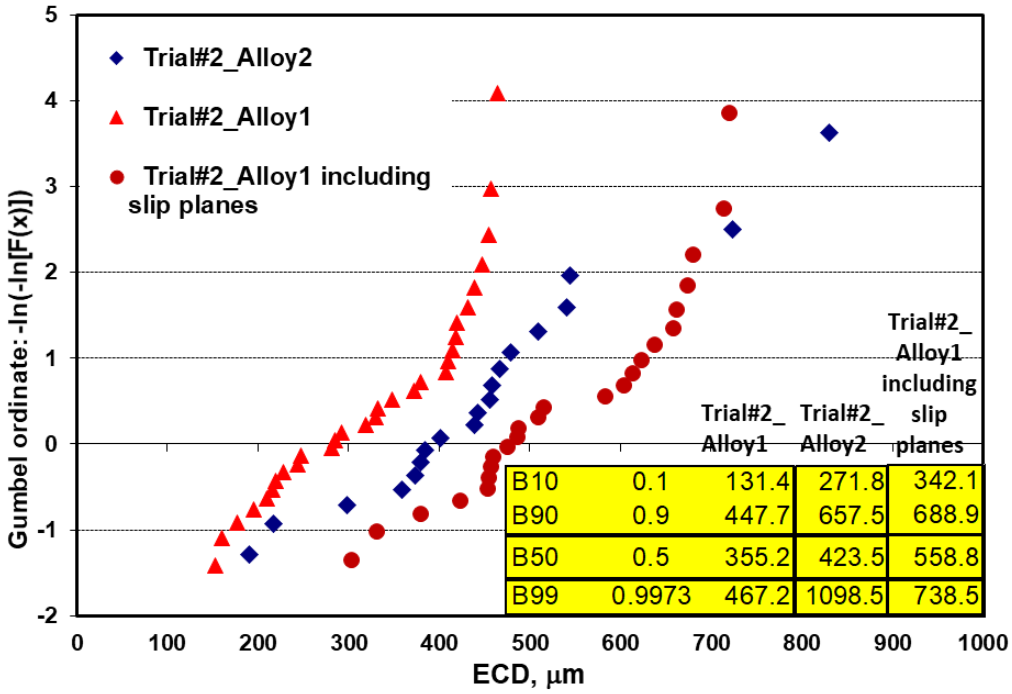

Figure 16. A comparison of size distributions of defects and shear planes that initiated fatigue cracks in the high-pressure oil line locations of engine heads made of both Alloy 1 and Alloy 2.

2.6 Low Cycle Fatigue Strength

A summary of the low cycle fatigue strength (10^4 cycles) is shown in Table 6. The newly developed alloy (Alloy 2 Trial 1 and Alloy 2 Trial 2) has comparable low cycle fatigue (LCF) with the baseline alloy (Alloy 1). This again indicates that the fatigue properties of cast aluminum alloys are strongly dependent upon defect sizes in the materials and to a much less degree upon on alloy matrix tensile strength.

Table 6. Low Cycle Fatigue strength (10^4 cycles) in engine cylinder heads.

Region	Test Temperature (°C)	Low Cycle Fatigue Strength (MPa)			
		Trial 1		Trial 2	
		Alloy 1	Alloy 2	Alloy 1	Alloy 2
Deckface and Combustion Chamber	25	N/A		218	220
	150	200	200	200	195
	200	N/A		137	132
	250	70	79	73	73
Bolt Boss	150	200	200	159	159
	200	N/A		129	126
	250	78	73	N/A	
High Pressure Oil Line	150	167	166	165	159
	200	N/A		113	117
	250	70	71	N/A	

2.7 Castability

The hot tearing tendencies are indicated by cracking susceptibility coefficients. The cracking susceptibility coefficient (CSC) is defined as:

$$CSC = \frac{t_v}{t_R}$$

where t_V is the time during solidification in which the casting is ‘‘vulnerable’’ to cracking, and t_R is the time available for the stress relief process. Following Clyne *et al*., [1] and Yan *et al*. [2], t_R is defined as the time spent during solidification when liquid volume fractions is between about 0.6 and 0.1 and t_V is the time spent when liquid volume fraction is between 0.1 and 0.01. Figure 17 shows the calculated CSC for Alloy 1 and Alloy 2. It is seen that both alloys have low hot tearing tendency and Alloy 2 is very comparable with Alloy 1.

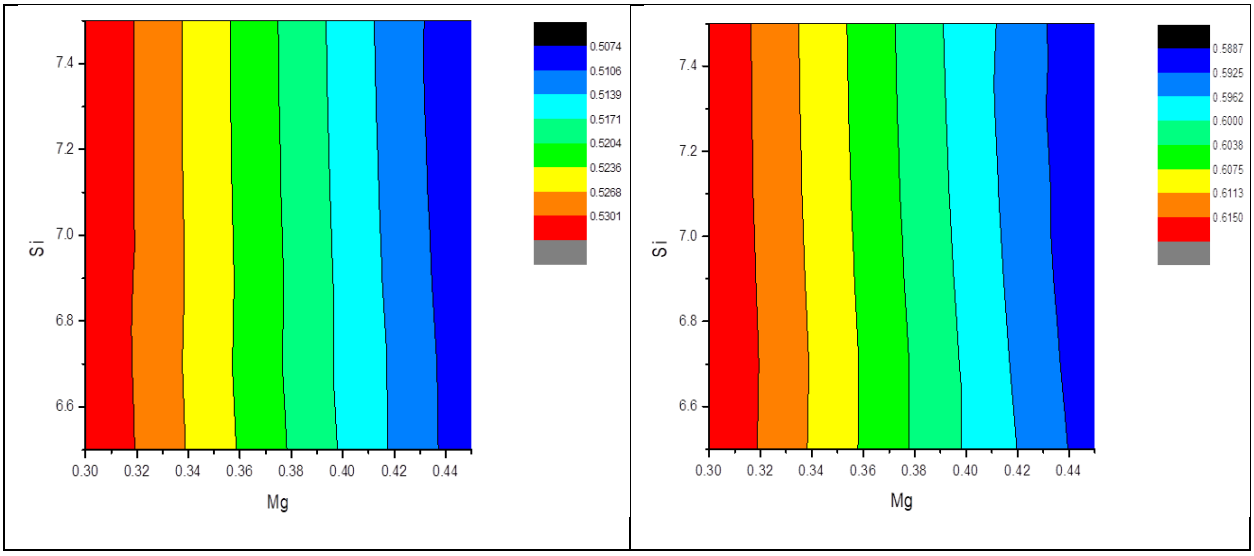

Figure 17 Contour plots showing the calculated hot tearing tendencies in (a) Alloy 1 and (b) Alloy 2.

Hot tear resistance and fluidity can be lumped together into the term “castability,” i.e. the ability to fill and produce a good casting. Castability also includes shrinkage and is often defined by criteria related to the fraction solid curve and solidification range. Shrinkage may also be affected by minor elements that precipitate during solidification and impede fluid flow during solidification. Since heads were produced in this project the best way to assess castability of the alloy is by X-ray of those heads. As shown in Table 5 the castability of the newly developed alloy appears better than the baseline A356 +0.5%Cu. Because the base for Alloy 2 was Alloy 1, however,these improved results are more likely a result of process variations such as improved cleanliness or reduced oxides. Nevertheless, what can be concluded is that the newly developed alloy has excellent castability and is comparable to standard production alloys such as A356.

Table 7. X-ray analysis of Trial 2 cylinder head castings.

	Alloy 1	Alloy 2
Number of Castings	35	49
Number of defects per 100 castings	43	6
Number of defect casting per 100 castings	31	6

2.8 Thermophysical Properties

Thermal property measurements including thermal diffusivity, specific heat, and linear thermal expansion were made on 12 specimens of Alloy 2 Trial 2. From these measurements, and bulk density calculated on the sample volume and mass, thermal conductivity and coefficient of thermal expansion were also calculated. The specimens were extracted from the chain guard region of twelve different heads after typical production heat treatment. The specimens were divided into 3 groups. The first group was tested at Room Temperature (RT), the second group was heated to 250°C for 200 hours and the third group was heated to 300°C for 200 hours prior to testing. Plots of thermal diffusivity, specific heat, thermal conductivity, and thermal expansion are shown in Figure 18-Figure 21. Additional thermophysical property details were provided in previously submitted milestone reports.

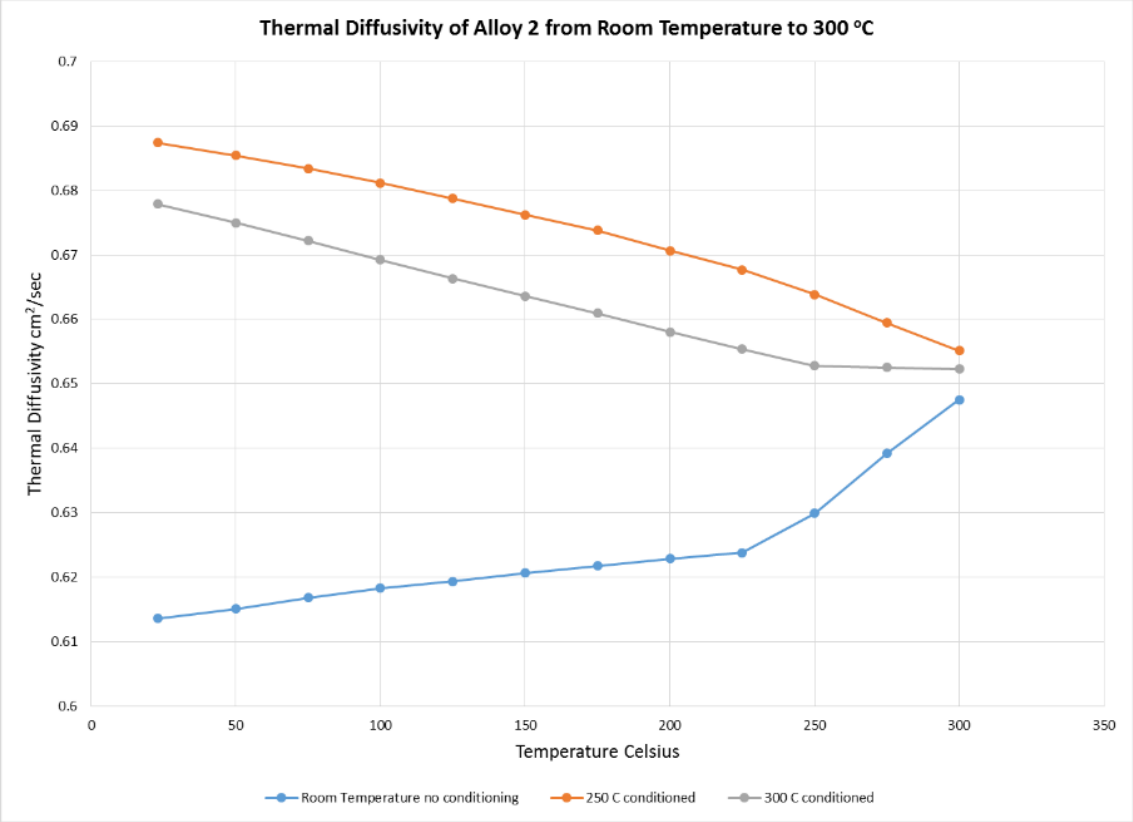

Figure 18. Measured thermal diffusivity of Alloy 2 cylinder head specimens

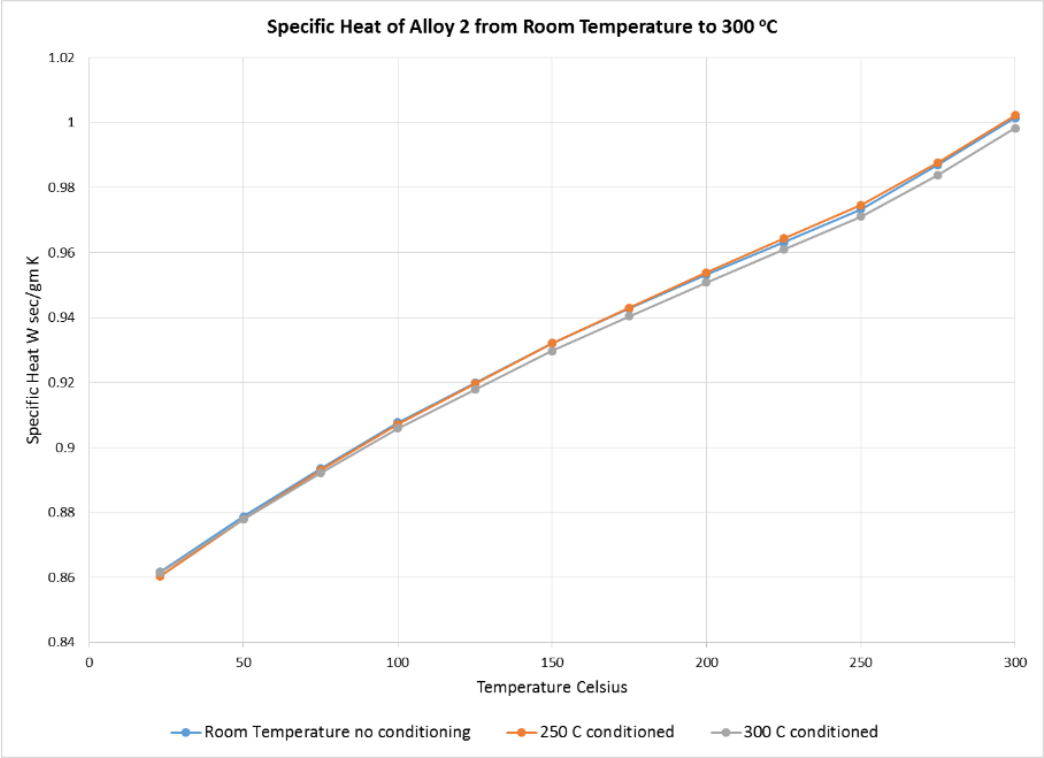

Figure 19. Measured specific heat of Alloy 2 cylinder head specimens

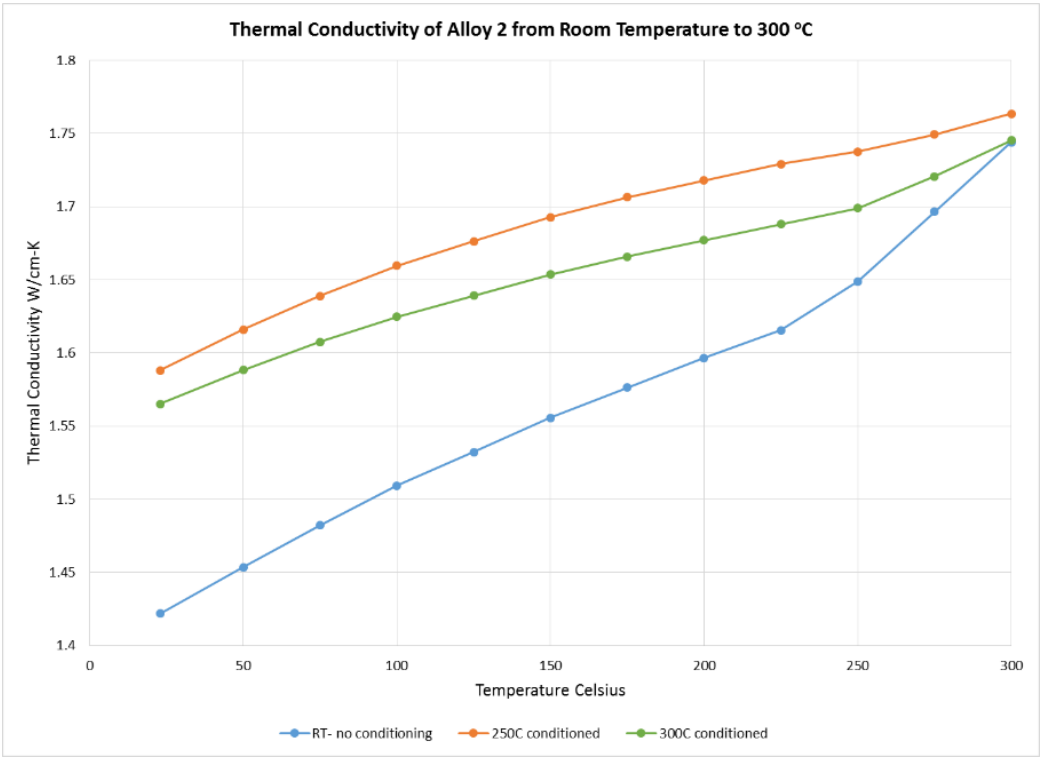

Figure 20. Measured thermal conductivity of Alloy 2 cylinder head specimens

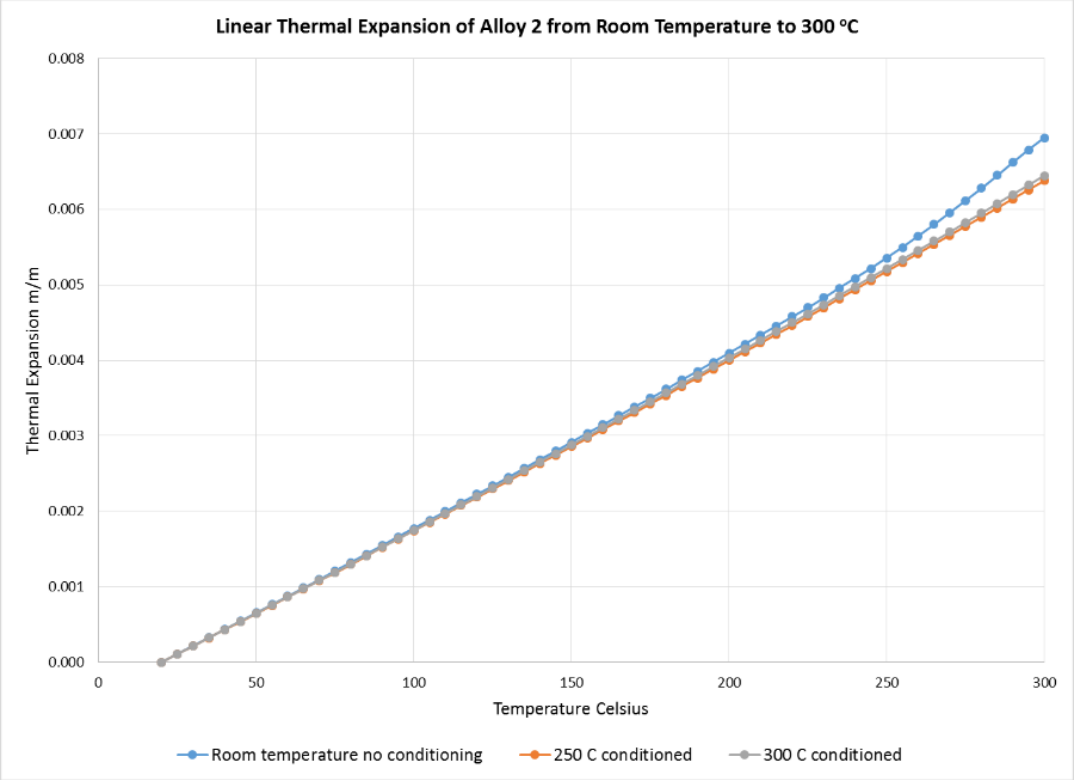

Figure 21. Measured thermal expansion of Alloy 2 cylinder head specimens

2.9 Thermophysical properties for solidification analysis

Thermophysical properties were not measured beyond 300ºC as current cylinder head operation is below this temperature. However estimates of these properties to the solidification temperature and using thermodynamic solidification models are sufficient for CAE solidification modeling. JMatPro® version 4.0 was used for these simulations. The calculated liquidus, solidus, and latent heat of solidification is shown in Table 8.

Table 8 Calculated properties of solidification

Property	Value
Liquidus temperature (Celsius)	605ºC
Solidus temperature	505ºC
Latent heat of Solidification	416 kJ/kg

The fraction solid versus temperature curve using Scheil solidification model is shown in Figure 22.

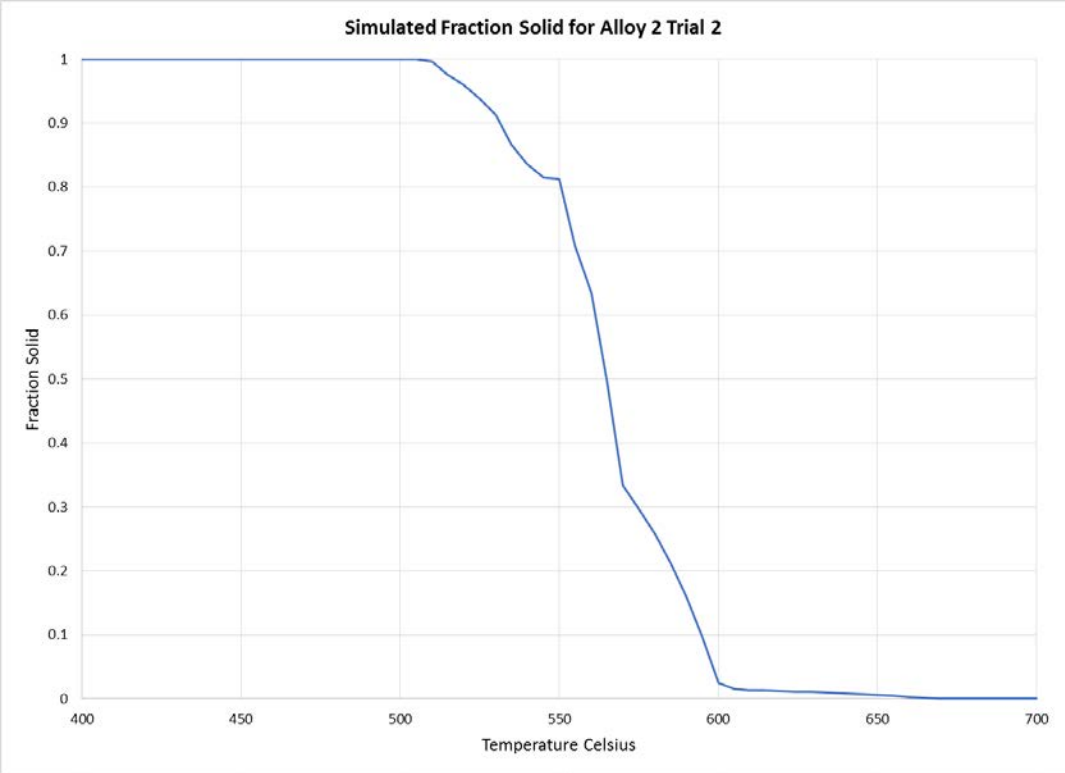

Figure 22 Calculated solid fraction curve for Alloy 2 Trial 2

The density of Alloy 2 Trial 2 is shown in Figure 23 along with the measured room temperature values. The difference between simulated density and measured density is about 2%.

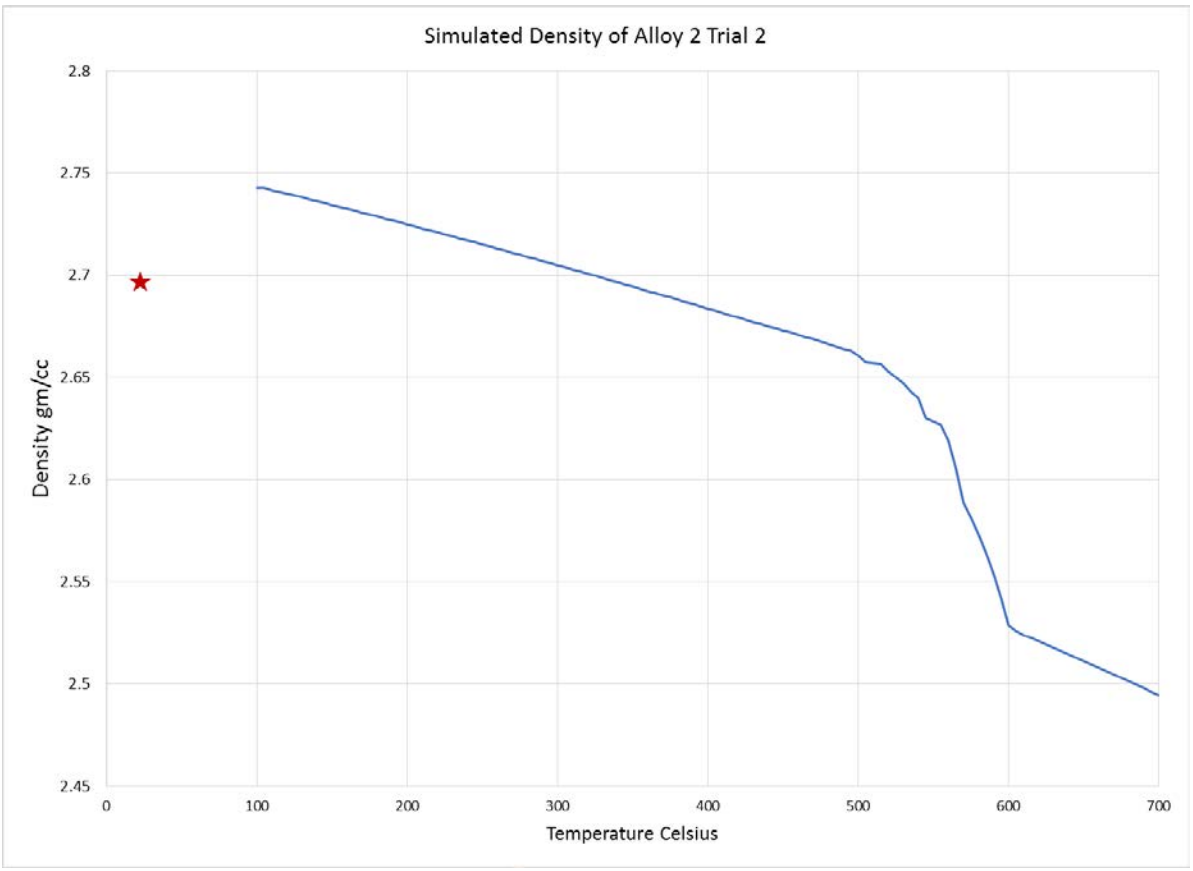

Figure 23 Simulated density of Alloy 2 Trial 2. The star indicates the measured value

The calculated thermal conductivity of Alloy 2 Trial 2 is shown in Figure 24. Also the measured thermal conductivity from room temperature to 300°C is included for comparison. This measured curve has been extended to the solidus using linear regression. The model calculation underestimates the thermal conductivity of the alloy in this case. However the condition of a solidifying and cooling alloy is also not equivalent to a heat treated alloy that was used in the measurement.

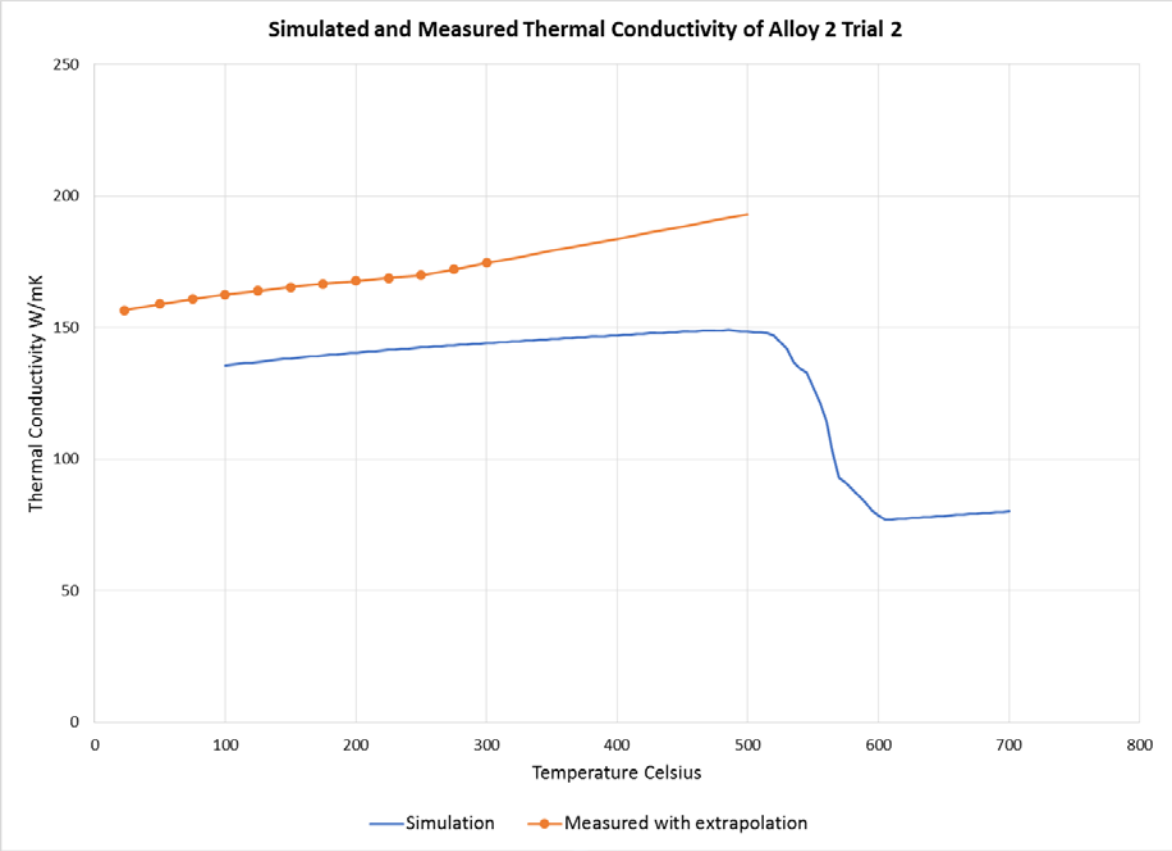

Figure 24 Simulated and measured thermal conductivity of Alloy 2 Trial 2

A comparison of the calculated and measured heat capacity of Alloy 2 Trial 2 is shown in Figure 25. Again the measured heat capacity was extended from 300°C to the solidus using linear regression. In this case the measurement matches very well with calculations for the temperature below 400oC. In JMatPro® the calculated heat capacity normally includes the latent heat of solidification. This was removed and the heat capacity value at the solidus was joined to the heat capacity value at the liquidus using linear interpretation.

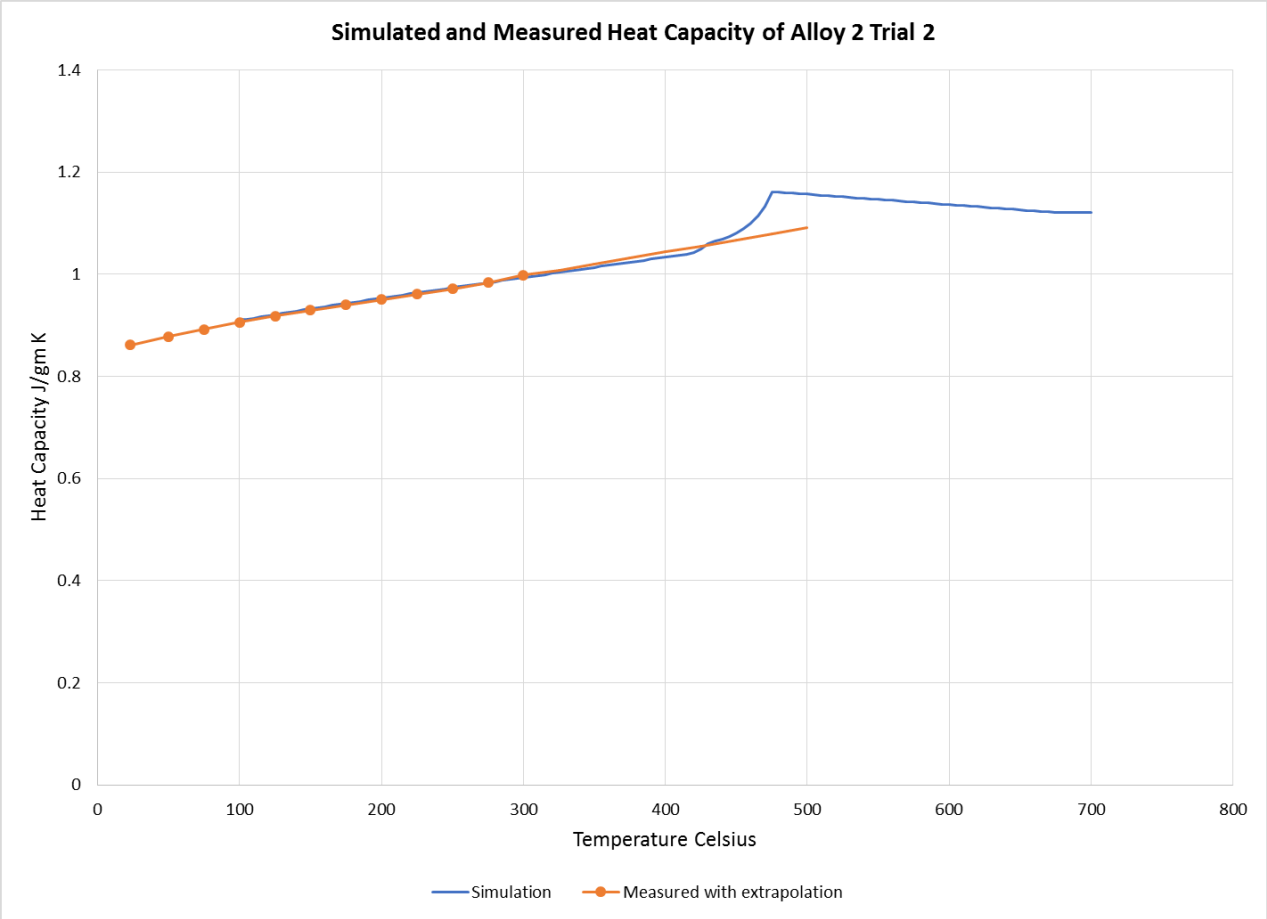

Figure 25 Simulated and measured heat capacity of Alloy 2 Trial 2

3. Overview of design concepts

3.1 Design using existing known precipitates

Based on a search of the literature and the use of QuesTek's ICME tools, concept alloys were generated for three strengthening precipitates: Q-phase, θ'-phase, and Mg2Si (β-phase). The θ'-phase is an Al-Cu phase which strengthens alloys like B319 containing Cu and shows excessive coarsening into more stable θ-phase at higher temperatures, resulting in poor high temperature strength. Cu-free alloys like A356 exhibit the formation of rod-shaped Mg_2Si β-phase precipitates, which have poor strengthening potency due to the coarse morphology of the β phase. The Q-phase is a quaternary Al-Si-Mg-Cu phase which has been gaining more scientific interest recently due to its superior high temperature stability to the theta phase, as well as the ability to refine the rod-shaped Q-phase microstructure through controlled solution and aging heat treatments.

The structure, morphology and composition of these precipitates phases have been researched widely (except Q-phase) and its knowledge is essential in designing the alloys. Using ICME tools like Thermo-Calc, designs incorporating these precipitates were proposed. Thermo-Calc is a software package that

implements CALPHAD (CALculation of PHAse Diagrams) methodology to perform thermodynamic and kinetic simulations to predict stable and meta-stable phase evolution in materials as a function of composition and processing. As discussed before, coarsening rate of the precipitate determines the high temperature strength of the alloy. The coarsening rates of the different types of potential precipitates need to be evaluated to establish the best candidate. The theory of diffusion-controlled precipitate coarsening was developed by Lifshitz and Slyozov and Wagner[3,4]:

$$\bar{R}^3 - \bar{R}_0{}^3 = Kt = \frac{8DC_e\gamma V_m{}^2 t}{9RT}$$

,

where D is the diffusivity and C_e is the equilibrium composition of the solute in the matrix. The "D x C" product of different alloying elements can be compared to determine the rate-controlling factor for a giving temperature. An expression for the multicomponent coarsening rate constant has been derived by Lee (et al.):

$$K_{Lee} = \frac{8\sigma V_m^{\beta}}{9RT}\left[\sum_{i\neq Fe}\left(\frac{X_i^{\beta}}{X_i^{\alpha}} - \frac{X_{Fe}^{\beta}}{X_{Fe}^{\alpha}}\right)\left(\frac{X_i^{\beta}}{X_i^{\alpha}} - 1\right)\frac{X_i^{\alpha}}{D_i^{\alpha}}\right]^{-1}.$$

The deciding factor can be simplified as:

$$\boldsymbol{D_i C_i^{\alpha}/X_i^{\beta 2}}$$

where α is the solution composition in the matrix and β represent specific precipitate.

Benchmark evaluations were performed on existing aluminum casting alloy compositions: B319, A354, A354+ and A356 (A354+ is a GM modification of A354).

Table 9. Compositions of the four benchmark alloys (wt.%)

Alloy	Si	Cu	Mg	Fe	Mn	Zn
B319	6.0	3.5	<0.1	<1.0		<3.0
A356	7.0	<0.2	0.35	<0.2		<0.1
A354	9.0	1.8	0.5	<0.2		<0.1
A354+	9.0	3.0	0.35-0.45	<0.2	0.6-1.0 Fe	<0.1

Table 9 shows the compositions of the benchmark alloys. The Fe and Zn are usually just residual content except for the case of B319, where the high Zn content contributes to the θ phase strengthening. Around 6~9 weight percent Si is added to the system for better eutectic solidification performance. The step diagrams (phase fractions vs. temperature) were calculated and plotted, as shown in Figure 26 which shows the evolution of the equilibrium phase fraction at different temperatures. Also, the incipient melting points of the alloys were calculated using the non-equilibrium Scheil simulation and are indicated with green dots along the temperature axis on the step diagrams.

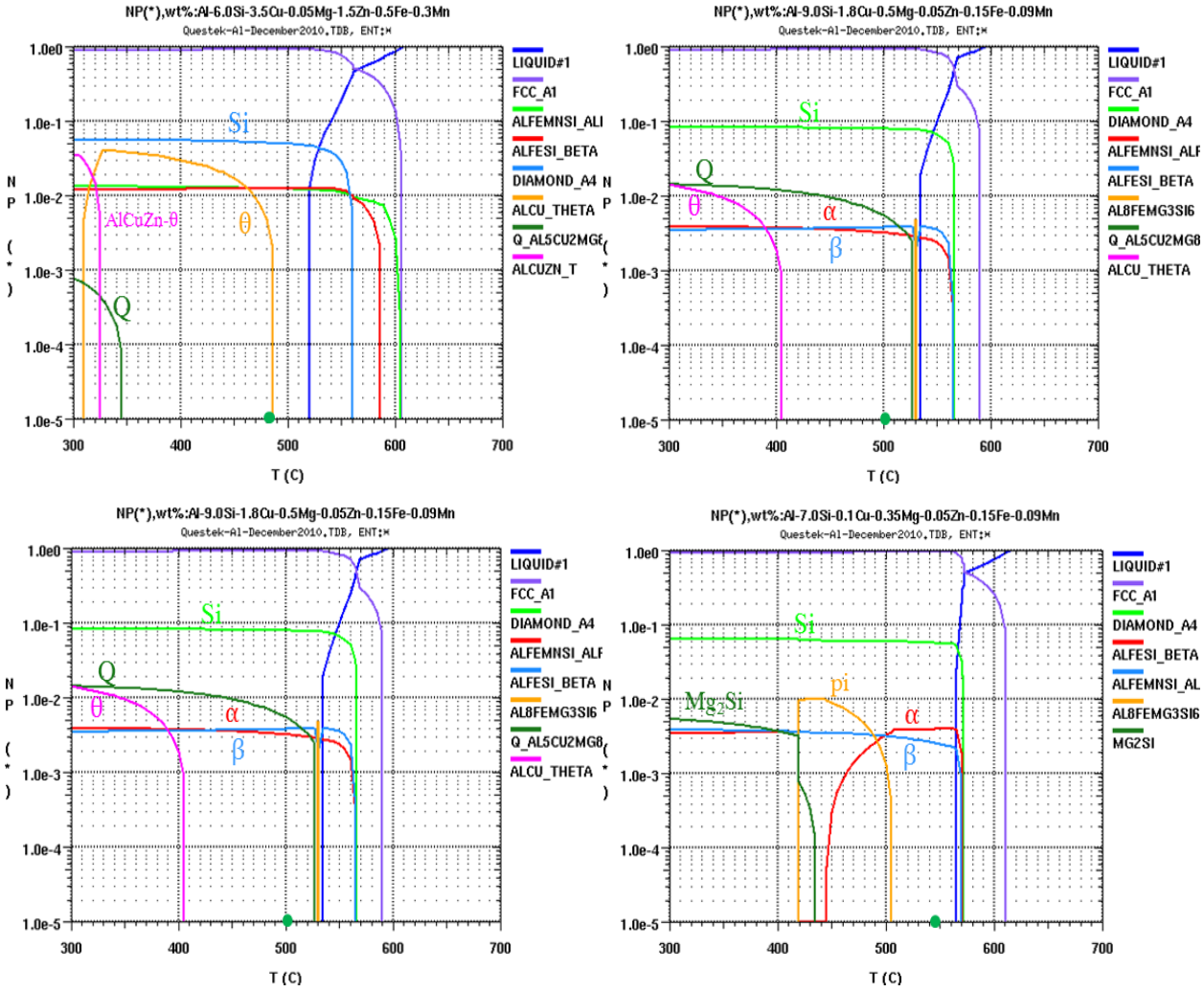

Figure 26. Equilibrium step diagrams of the four benchmark alloys (top left: B319, top right: A354, bottom left: A354+, bottom right: A356). The green dots indicate the incipient melting temperature determined from the non-equilibrium Scheil solidification simulation

Table 10 shows the "D x C" product of these benchmark alloys, which employ different strengthening precipitates. Since the "D x C" product does not take into account the difference between different precipitates, these results only provide a qualitative evaluation for the contributions of different alloy elements.

Table 10. "D x C" product of different benchmark alloys (units of m2/s)

	D x C (m^2/s)				
Alloy	**Si**	**Cu**	**Mg**	**Zn**	**Al**
B319	4.62E-20	1.04E-19	4.86E-20	1.06E-18	1.93E-17
A354	4.75E-20	1.09E-19	4.71E-20	6.97E-20	1.91E-17
A354+	4.75E-20	1.09E-19	4.71E-20	6.92E-20	1.91E-17
A356	4.66E-20	2.62E-20	6.42E-20	6.98E-20	1.95E-17

Compared with the different strengthening precipitation mechanisms, the quaternary Q-phase shows better high temperature stability, thus the design work is first focused on the Q-phase strengthened aluminum. To optimize the stability and coarsening resistance of the Q-phase precipitate, a thermodynamic tie-line

approach is sought to evaluate the variation of the matrix composition in equilibrium with Q-phase, which is illustrated in Figure 27. The composition range of the FCC matrix is found within the two corners (FCC HCu and FCC LCu) of the green wedge shape phase field in the Al-Si-Cu-Mg quaternary pyramid. The FCC HCu is in equilibrium with Al_2Cu (θ phase) while FCC LCu is in equilibrium with Mg_2Si.

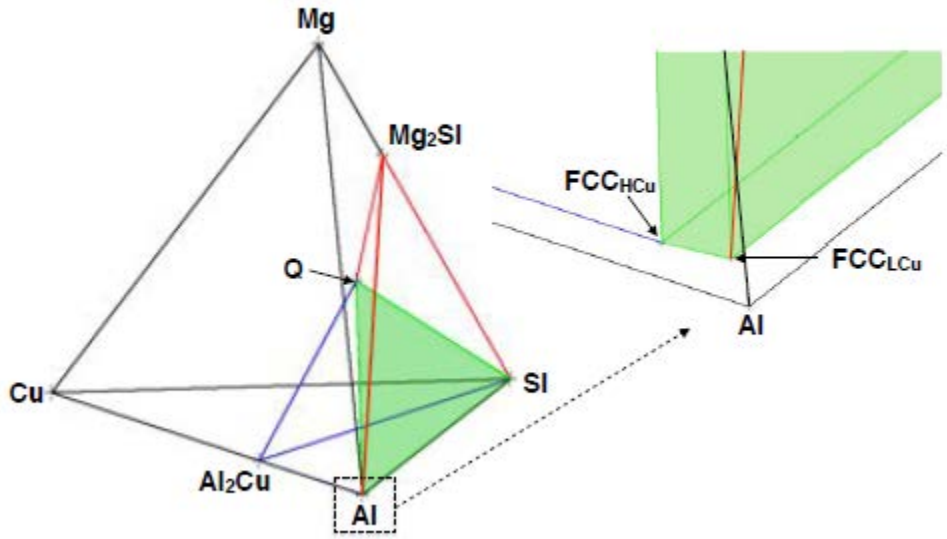

Figure 27. Schematic of the FCC-Si-Q equilibrium region. The FCC HCu is in equilibrium with Al¬2Cu (θ phase) while the FCC LCu is in equilibrium with the Mg2Si.

Due to relatively mature thermodynamic description of the θ'-phase and β-phase, optimum cast alloy designs were proposed directly. However for Q-phase designs, three low-Si wrought design were proposed to facilitate evaluation of these alloys in 3D Atom Probe Tomography (APT) studies for understanding Q-Phase stability which at the beginning of the project was not fully described in the thermodynamic databases. Along with single precipitate concepts, dual precipitate concepts such as "Castalloy TQ," which included both θ + Q-phase, were also designed.

- 3 button designs:
  - QAlloy 1 Al-0.83Cu-0.52Si-0.56Mg-(0.05Zn-0.15Fe-0.09Mn)
  - QAlloy 2 Al-0.92Cu-0.65Si-0.71Mg-(0.05Zn-0.15Fe-0.09Mn)
  - Qalloy3 Al-0.45Cu-0.65Si-0.52Mg-(0.05Zn-0.15Fe-0.09Mn)
- 4 casting designs:
  - CastalloyQ Al-0.76Cu-5.9Si-0.48Mg-(0.05Zn-0.15Fe-0.09Mn)
  - CastalloyT Al-2.81Cu-5.34Si-(0.03Mg-0.05Zn-0.15Fe-0.09Mn)
  - CastalloyTQ Al-3.04Cu-5.53Si-0.3Mg-(0.05Zn-0.15Fe-0.09Mn)
  - CastalloyM Al-0.1Cu-7.13Si-0.63Mg-(0.05Zn-0.14Mn, <0.1Fe)

The compositions are in weight percent and the content in the parentheses is regarded as acceptable residual level. The name of the button designs indicates they are derivatives of Q-phase strengthened but with different precipitate fraction or matrix composition. The casting alloys include more Si to improve the castability, with "CastalloyQ" as Q-phase strengthened, "CastalloyT" as θ-phase, "CastalloyTQ" as Q and

θ-phase combined and "CastalloyM" as Mg_2Si. CastalloyM is designed based on A356 while all the other designs are based on calculations performed on A354/A534+. The deciding factor ("DC/X^2") for the coarsening rate of different strengthening precipitates was calculated and listed in Table 11. It shows Mg is usually the deciding factor for coarsening due to its lowest DC/X^2 value, except for Qalloy3, in which Si is the lowest.

Table 11. DC/X^2 value of the design alloys (units of m^2/s).

	DC/X^2 (m^2/s)				
Alloy	**Si**	**Cu**	**Mg**	**Zn**	**Al**
QAlloy 1	5.71E-19	1.20E-17	3.29E-19	8.30E-12	3.37E-16
QAlloy 2	5.72E-19	1.20E-17	3.29E-19	8.25E-12	3.37E-16
Qalloy3	2.94E-19	7.14E-18	6.19E-19	3.22E-11	3.40E-16
CastalloyQ	5.81E-19	1.20E-17	3.25E-19	8.35E-12	3.37E-16
CastalloyT	5.81E-19	1.20E-17	3.25E-19	8.54E-12	3.37E-16
CastalloyTQ	5.81E-19	1.20E-17	3.25E-19	8.49E-12	3.37E-16

Samples were cast at GM, with the two Qalloy concepts produced as buttons and the CastalloyQ as a two-inch plate casting. Following detailed process optimization studies, each alloy was homogenized/solutionized and quenched to reduce microsegregation. A detailed aging study was completed in the target aging temperature range to assess the precipitation response of the concept alloys. Isothermal aging studies were performed to confirm the precipitation strengthening behavior in these alloys. Results from process modeling and aging studies are presented in Section 2 of this report.

3.2 High throughput DFT identified novel Heusler-phase precipitates

Collaborations between QuesTek and Professors Chris Wolverton and Peter Vorhees at Northwestern University were established to begin high-throughput searches for previously unknown precipitate phases. The Wolverton group's Open Quantum Materials Database (OQMD), a database which includes the results from density functional theory (DFT) calculations for a wide range of structures, was utilized to identify possible strengthening phases. This database includes calculations of all possible elemental combinations of many structural prototypes, including B1, B2, B3, B4, B19, Bh, L10, L11, L12, D019, D022, Perovskite, brownmillerite, and Heusler structures, as well as all structures (but not all elemental combinations) from the Inorganic Crystal Structure Database (ICSD).

The high-throughput search was developed to target possible stable structures in cast aluminum. Thus, the search only included the lowest energy (via DFT) structures for a given composition. This list was then screened for stability with elements in the base alloy including aluminum, silicon, copper, and magnesium (i.e., structures were required to have an un-interrupted tie-line on the multi-component convex hull with fcc aluminum). This criteria was enforced to ensure that a given structure would not decompose into other phases. Additionally, radioactive, precious, toxic, and reactive elements were excluded. Finally, as structural entries the OQMD database are labeled by space group, the initial search was restricted to structures in the 221 space group. The motivation behind this was to find a replacement for Al3Sc, structure type L12 (space group 221). Once structures which satisfied these requirements were found, they were sorted based on the lattice constant mismatch with Al_{fcc}. Precipitate structures with lower lattice constant mismatch are known to be more potent strengtheners.

The 221 space group search yielded several results. Sorted in order of lattice constant matching (up to 10% lattice mismatch), they include: $ScGa_3$, $ScAl_3$, $ErGa_3$, $LuGa_3$, $LuAl_3$, $TmAl_3$, $TmGa_3$, $HoGa_3$, $DyGa_3$, and

$TbGa_3$. Unfortunately, this list includes gallium (Ga), a known grain boundary embrittler in aluminum. Other members include thulium and lutetium which are both rare and far too expensive for the present applications. It is promising to note that this search did include the known strengthening phase Al3Sc. However, notable metastable phases not included include Al3Er and Al3Yb. These structures have been experimentally identified, and were predicted not to be stable in the DFT calculations. Due to this omission, a promising avenue will be to include metastable phases which are a certain distance from the convex hull in future HT DFT searches. The HT DFT search was next expanded to include all cubic structures. In this search, three possible stable precipitates were identified. These are listed below along with lattice constant mismatches and number of cell repetitions with respect to FCC-Al:

- $Al_{12}X$ structures (X = Re, Mo, Mn, W) (bcc); $Al_{12}Mn$ is selected due to solubility of Mn in Al
- $Al_{18}Mg_3Ti_2$ (fcc)

As strengthening precipitates for high temperature (250°C and above) applications are sought in this project, a key aim is to slow the coarsening rate of these precipitates. This can be related to the elemental relative diffusivity in aluminum of these phases. Figure 28 shows the relative diffusivities of the elements with respect to aluminum. Note the low diffusivities of Cr, Mn, and Ti. Given these low values, this should encourage slow coarsening at higher temperatures. Initial button designs were developed targeting a 2% volume fraction of precipitates in aluminum. These designs were given to GM for melting –

- AlMnDFTalloy Al-0.30Mn
- AlTiMgDFTalloy Al-0.23Mg-0.30Ti
- AlCrSiDFTalloy Al-0.36Cr-0.2Si

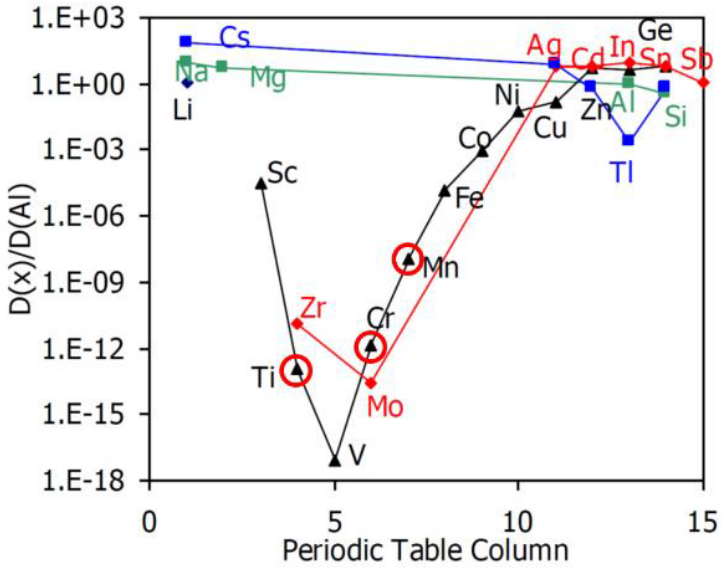

Figure 28. Relative diffusivities of target elements versus aluminum

3.3 Elemental additions to improve coarsening resistance of Q-phase

To improve coarsening resistance of precipitates, slow diffusing elemental additions that would result in solute partitioning at the precipitate-matrix interface are sought. DFT calculations were performed in order to determine solute partitioning of elements to the Q-phase precipitate. Initial calculations optimized the Q-phase structure and determined the vacancy defect energies of removing selected atoms from this phase. Energies were calculated for Mg-rich structure and Cu-rich structure. These energies and nearest neighbor properties are shown in

Figure 29. Energies indicate that no vacancies were favorable; however, vacancy defect energies were lowest (i.e. most favorable) on the two Cu-based sublattices. As these sites had the shortest nearest-neighbor distances, this result is likely due to a local volume effect and not necessarily related to the behavior of the electronic structures, e.g. bonding effects.

Following this, calculations were performed to determine the partitioning energies of solute atoms using DFT. Partitioning energies are defined as the energy difference of inserting a solute atom in the Al-fcc phase minus the energy of adding that atom to the Q-phase. A negative value of partitioning energy implies a favorable partitioning of the element to the precipitate phase and vice versa for positive. The DFT results (Figure 30) for the various solute elements indicate that Zn, Ag, Au, Ni, Co, Sr, Ba, Ga, Ge, Sn, and Sb partition to the Q-phase. To experimentally validate the partitioning effect using 3D-APT, alloys with small addition of V, Mn, Ti and Zn were cast.

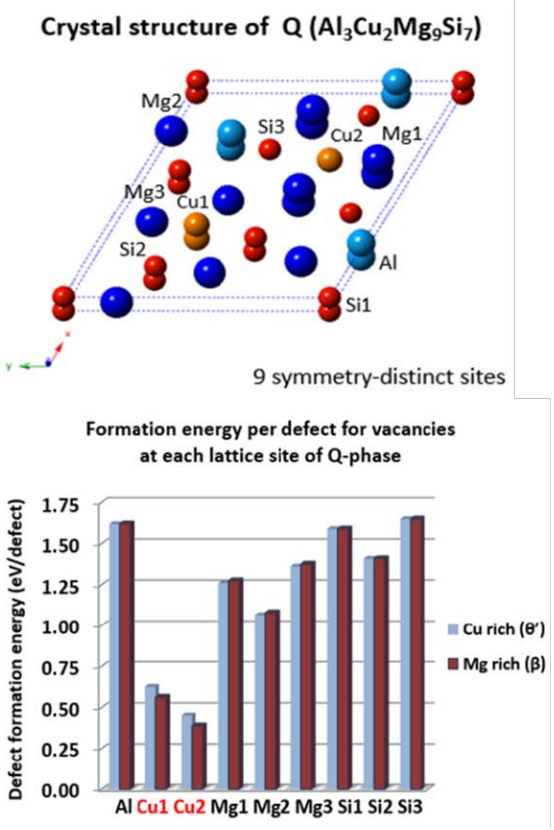

Site	Nearest elements	Mean distance of 3 nearest atoms
Al	Si	2.545Å
Cu1	**Si**	**2.362Å**
Cu2	**Si**	**2.376Å**
Mg1	Si1, Cu2	2.737Å
Mg2	Si1, Cu2	2.684Å
Mg3	Si	2.779Å
Si1	Al	2.586Å
Si2	Cu1, Al1, Mg1	2.534Å
Si3	CU1, Al2	2.492Å

Figure 29. (Left-top) The crystal structure of the Q-phase as used in DFT calculations. (Left-bottom) Defect formation energy for vacancies in the Q-phase. (Right) Table showing the NN distances and elemental species of each of the atomic sites of the Q-phase

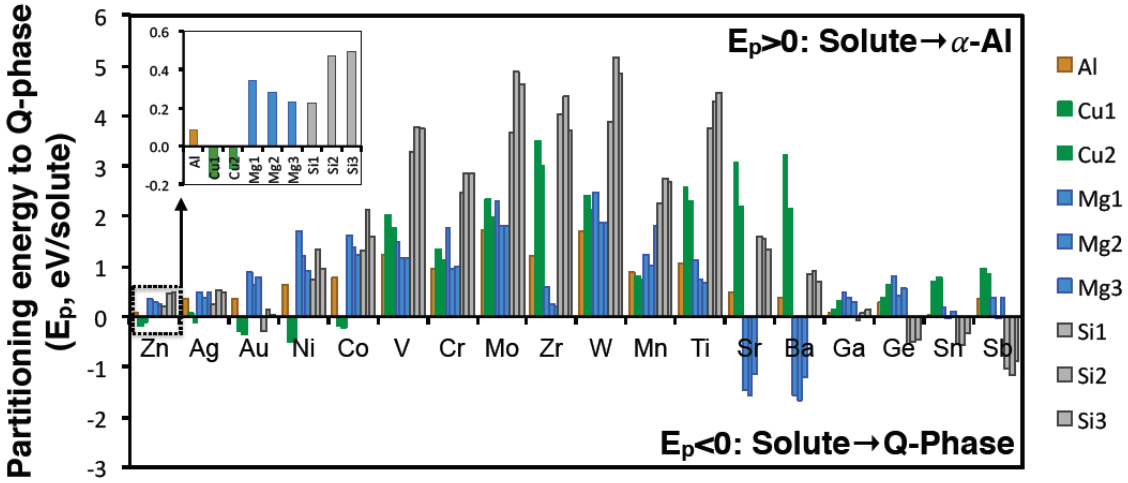

Figure 30. Partitioning energy of various solute to the Q-phase. A negative (or positive) value indicates the solute prefers locating into a sub-lattice of Q-phase (or fcc-Al)

Button scale alloys were cast for each of these elemental additions for the case of both Q and TQ alloys as shown in Table 12. Isothermal studies were performed on each alloy to see the effect of solute partitioning on long-term aging.

Table 12. Composition of elemental addition designs

	Al	Cu	Si	Mg	Zn	Fe	Mn	Ni	Co	V	Ti	Zr
Wrought Q	BAL	0.733%	0.518%	0.566%	0.050%	0.150%	0.090%	0.000%	0.000%	0.000%	0.000%	0.000%
+Mn	BAL	0.733%	0.518%	0.566%	0.050%	0.150%	0.250%	0.000%	0.000%	0.000%	0.000%	0.000%
+Ni	BAL	0.733%	0.518%	0.566%	0.050%	0.150%	0.090%	0.100%	0.000%	0.000%	0.000%	0.000%
+Co	BAL	0.733%	0.518%	0.566%	0.050%	0.150%	0.090%	0.000%	0.050%	0.000%	0.000%	0.000%
+V	BAL	0.733%	0.518%	0.566%	0.050%	0.150%	0.090%	0.000%	0.000%	0.150%	0.000%	0.000%
+Ti	BAL	0.733%	0.518%	0.566%	0.050%	0.150%	0.090%	0.000%	0.000%	0.000%	0.150%	0.000%
+Zr	BAL	0.733%	0.518%	0.566%	0.050%	0.150%	0.090%	0.000%	0.000%	0.000%	0.000%	0.150%
+Zn	BAL	0.733%	0.518%	0.566%	0.200%	0.150%	0.090%	0.000%	0.000%	0.000%	0.000%	0.000%
Wrought TQ	BAL	3.060%	0.650%	0.300%	0.050%	0.150%	0.090%	0.000%	0.000%	0.000%	0.000%	0.000%
+Mn	BAL	3.060%	0.650%	0.300%	0.050%	0.150%	0.250%	0.000%	0.000%	0.000%	0.000%	0.000%
+Ni	BAL	3.060%	0.650%	0.300%	0.050%	0.150%	0.090%	0.100%	0.000%	0.000%	0.000%	0.000%
+Co	BAL	3.060%	0.650%	0.300%	0.050%	0.150%	0.090%	0.000%	0.050%	0.000%	0.000%	0.000%
+V	BAL	3.060%	0.650%	0.300%	0.050%	0.150%	0.090%	0.000%	0.000%	0.150%	0.000%	0.000%
+Ti	BAL	3.060%	0.650%	0.300%	0.050%	0.150%	0.090%	0.000%	0.000%	0.000%	0.150%	0.000%
+Zr	BAL	3.060%	0.650%	0.300%	0.050%	0.150%	0.090%	0.000%	0.000%	0.000%	0.000%	0.150%
+Zn	BAL	3.060%	0.650%	0.300%	0.200%	0.150%	0.090%	0.000%	0.000%	0.000%	0.000%	0.000%

4. Experimental Results and Analysis

4.1 Results for Q-phase, θ'-phase and β'-phase alloys

To better understand and model the Q-phase, Q-Alloy 2 design was used to perform a detailed experimental characterization of the alloy. Presence and aging of Q-phase was confirmed as shown in Figure 31 with peak aging occurring somewhere between 4-8 hrs.

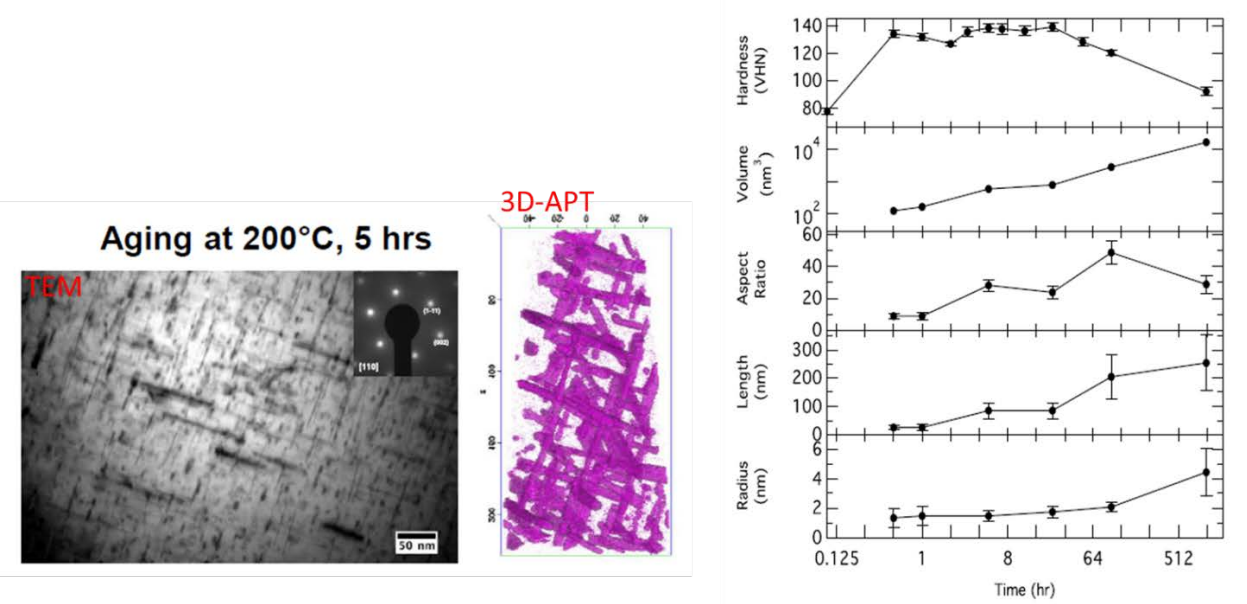

Figure 31. (left) TEM and 3D-APT micrographs of Q-Alloy 2 showing rod-shaped Q-phase precipitates. (right) Evolution of Q-phase at 200C in QAlloy 2

Isothermal aging studies at high temperature (200˚C and 250 ˚C) were performed on all the castalloy designs. CastalloyTQ demonstrated the highest strength at both the temperatures followed by CastalloyQ as shown in Figure 32. CastalloyM and CastalloyT underperformed and were abandoned from further evaluation. Tensile test of CastalloyTQ showed poor plastic elongation while CastalloyQ showed optimum elongation (Figure 33). However, it was noted that superior room temperature property did not translate completely to the better high temperature strength, as can be seen in Figure 33 where the strength at 300 C for all the alloys were very similar in contrast to the room temperature strength. These strength and microstructural characterization data was used to calibrate the thermodynamic database and the strength model for these alloys (discussed in the subsequent sections).

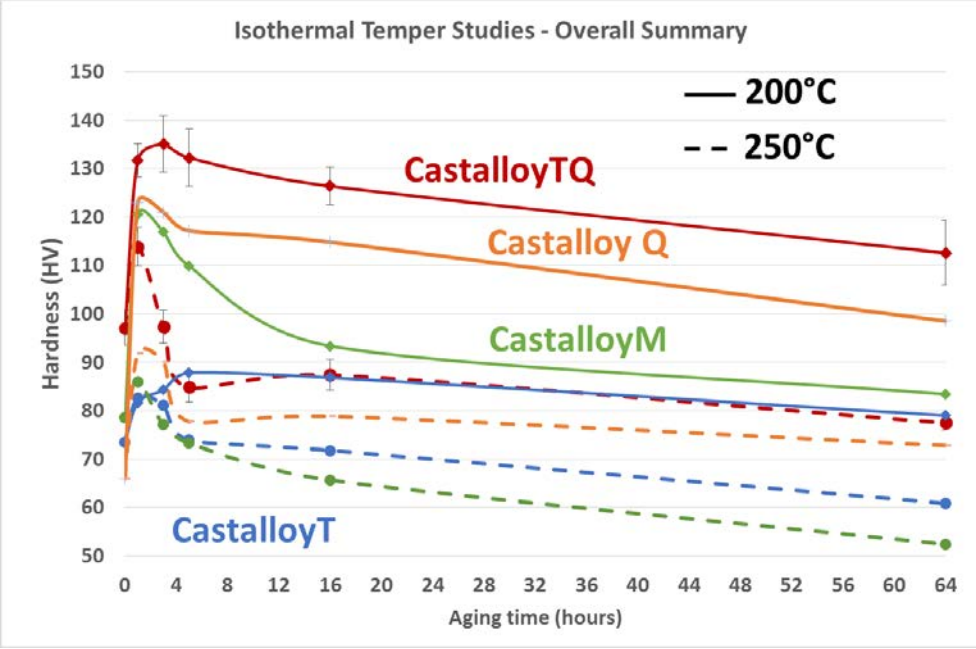

Figure 32. Isothermal aging study for castalloy designs at 200ºC and 250ºC.

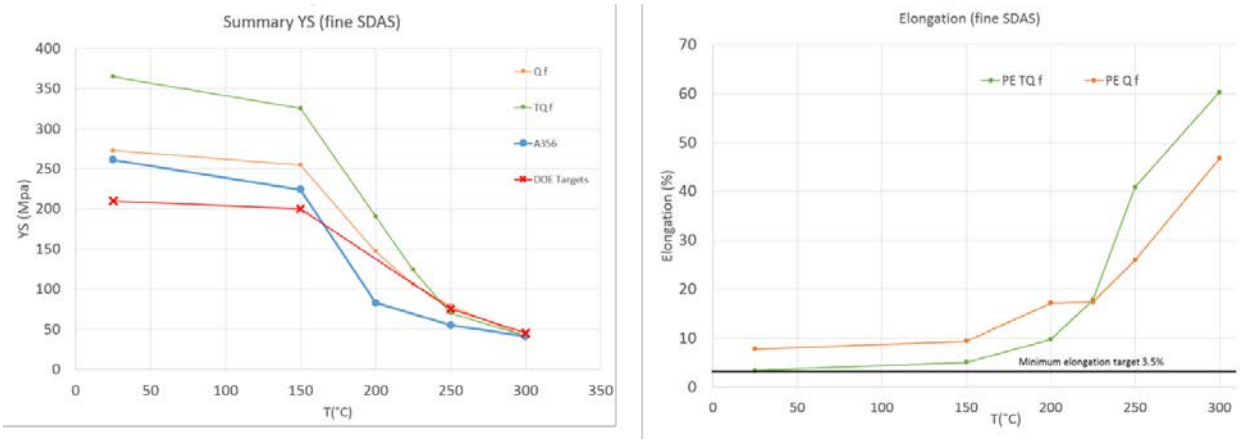

Figure 33. Tensile test results for CastalloyQ and CastalloyTQ at different test temperatures

4.2 Results from HTDFT novel precipitate designs

An isochronal and isothermal aging study was performed at QuesTek for three DFT concept alloys: HT-DFT-Mn, HT-DFT-Ti, and HT-DFT-Cr (Figure 34 and Figure 35). These alloys were aged for 1 hour at 200, 300, and 400°C after homogenization, and the isothermal results were for 300°C aging. There was no clear precipitation strengthening effect in the isochronal results. For the Mn- and Ti-based alloys, there seems to be a softening at higher heat treatment temperatures. For each prototype, there is a hardening with the solution treatment (SHT). However, after this hardening is achieved for each of these alloys, there is no measurable peak in the isochronal results beyond experimental uncertainty.

An isothermal hardness study was subsequently performed at 300°C for each of these alloys (see Figure 35). Here a peak is measured in the Ti-based button occurring at 16 hours. However, this peak is within experimental uncertainty, and is not observed for the other button alloys. No hardness peak was observed

for either the Cr-based or Mn-based samples suggesting that precipitate formation and growth is not occurring.

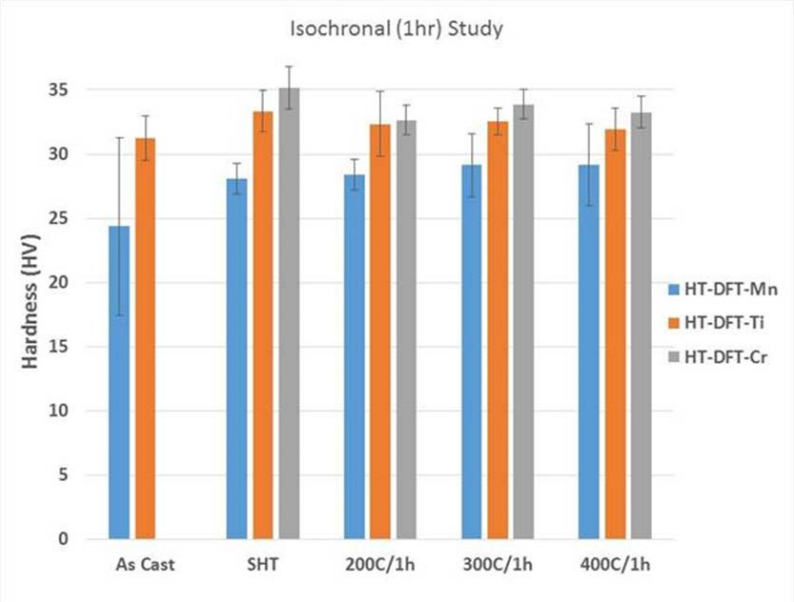

Figure 34: Isochronal hardness study of HT-DFT alloys.

While these results are not very promising for secondary precipitate hardening, they may be evidence of the possibility of solid solution strengthening for these alloys. Additional LEAP/3D-APT work can help in identification of the location of Ti, Mn, and Cr atoms with these samples and/or if any precipitation was exhibited in these alloys.

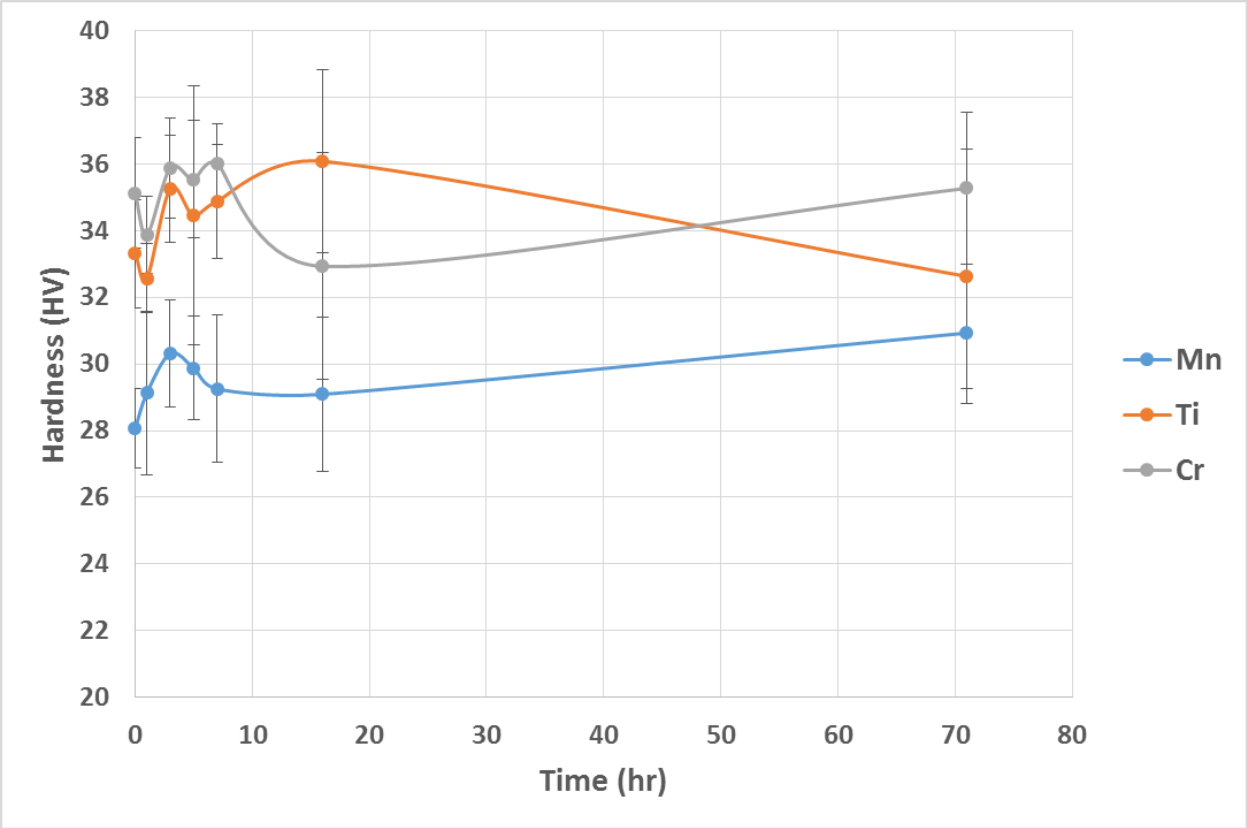

Figure 35: Isothermal hardness study of HTDFT alloys at 300°C. Hardening peaks fall within margin of error in the current isothermal study.

4.3 Results from elemental addition designs

The elemental addition alloys were solutionized (WQ: 495-580C for 49h; WTQ: 495-525C for 48h) and then aged at 200°C for various times. Results of microhardness for alloy Q additions can be found in Figure 37, while microhardness results for alloy WTQ can be found in Figure 36. In alloy WQ, it was found that Zr, Mn, and Zn additions may slow coarsening. In alloy WTQ, it was found that V, Mn, and Zn may slow coarsening.

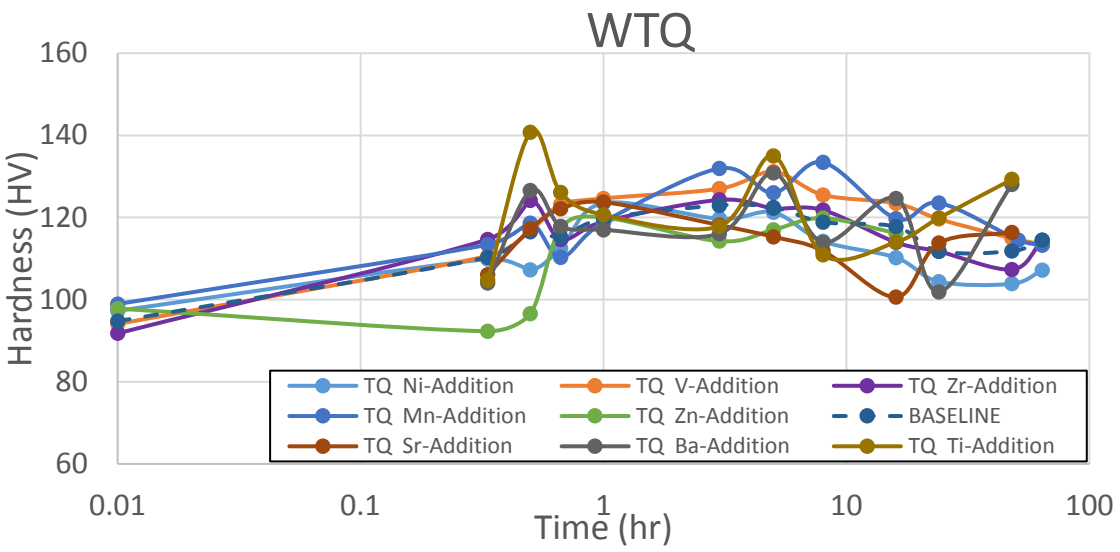

Figure 36 Microhardness measurements versus time for 200°C aging of wrought alloy TQ with various alloying additions

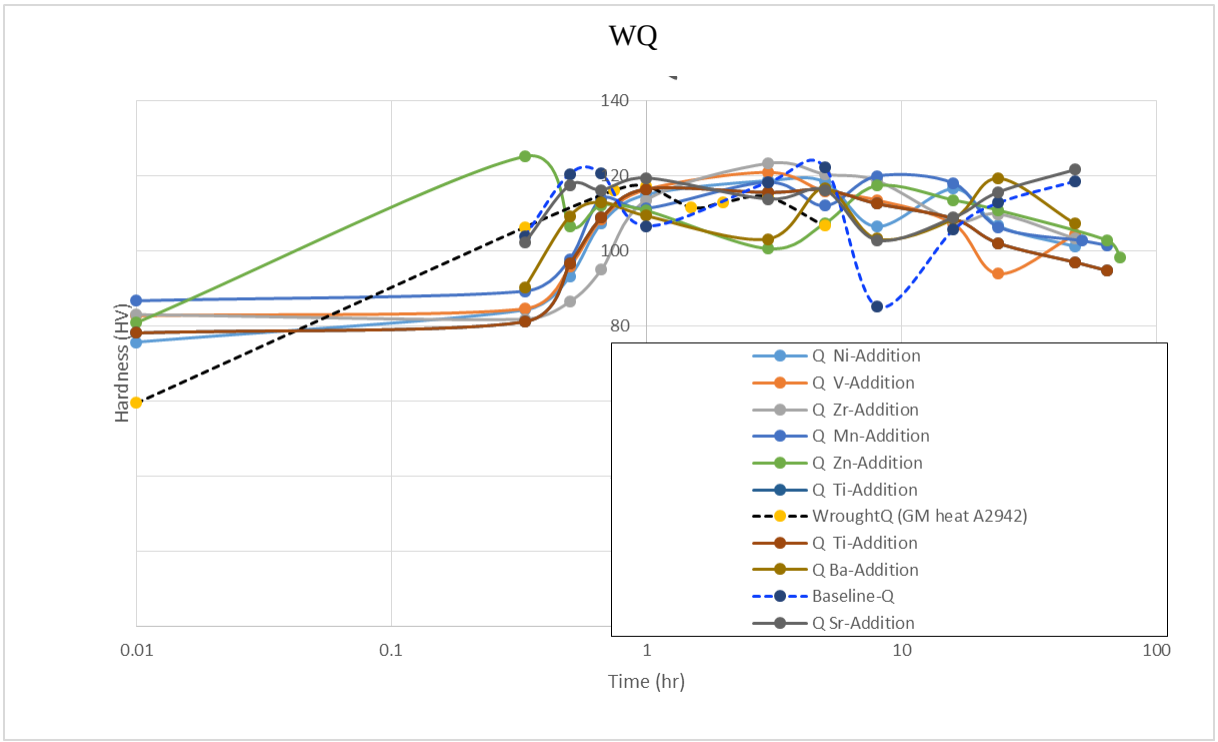

Figure 37 Microhardness measurements versus time for 200°C aging of wrought alloy Q with various alloying additions

Further investigation by 3D-APT/ LEAP shows favorable partitioning of Zn, Ni and Mn to the Q-phase as predicted by DFT calculations. Figure 38 shows the 3D-APT/ LEAP reconstruction from elemental

additions to alloy WQ. It can be seen from the reconstructions that addition of partitioning elements helps in slowing the coarsening of the precipitates as compared to the case of WQ (Figure 38 (a)). Figure 39 shows the proxigram results from the LEAP analysis of WQ + (Zn, Ni and Mn) alloys showing enrichment of these elements at the interface of the Q-phase precipitate. On a contrary, Figure 40 shows the proxigram for Ti, V and Zr that also seem to partition to Q-phase but were predicted not to by DFT calculations. Slow diffusivities of these elements combined with the observed segregation effect can help in slowing the coarsening of the Q-phase in these alloys.

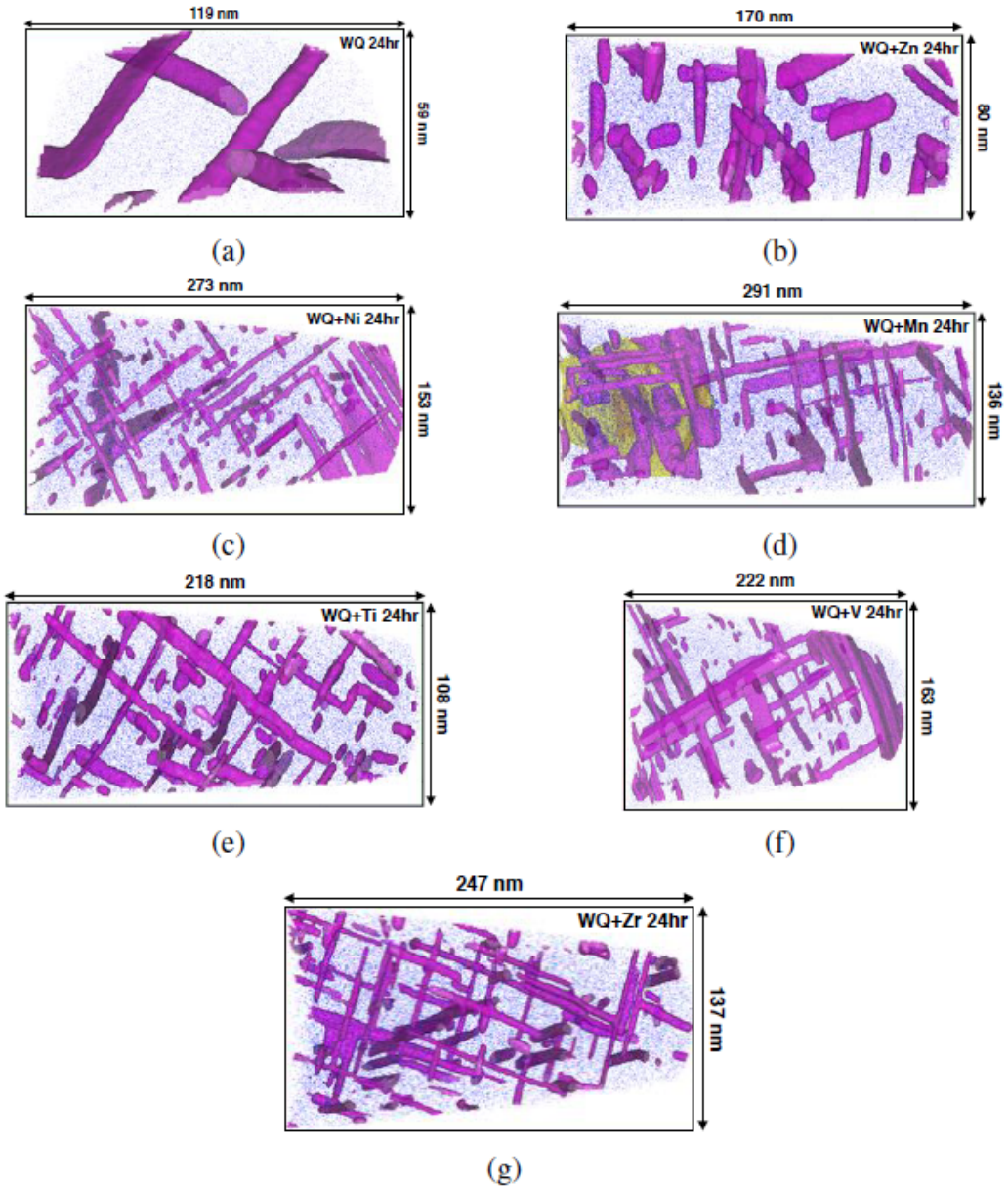

Figure 38. 3D-APT/ LEAP reconstruction for the WQ addition alloys aged at 200oC for 24 hrs. Al atoms are shown in blue, Q-phase outlined using 7% Mg+Si is-surfaces, and Fe-Mn intermetallic particle shown

in yellow with a Mn iso-surface. (a) WQ, (b) WQ+Zn, (c) WQ+Ni, (d) WQ+Mn, (e) WQ+Ti, (f) WQ+V and (g) WQ+Zr

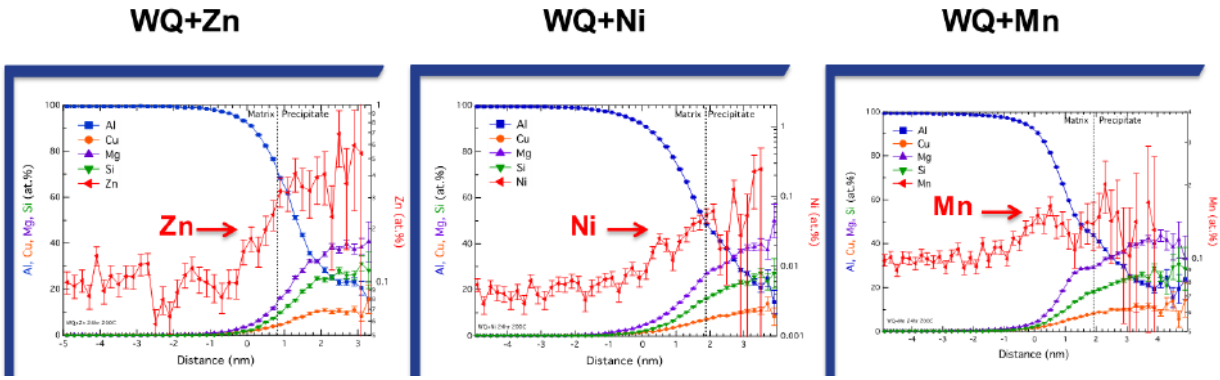

Figure 39. Proxigram results for Zn, Ni and Mn partitioning into Q-phase as predicted by DFT

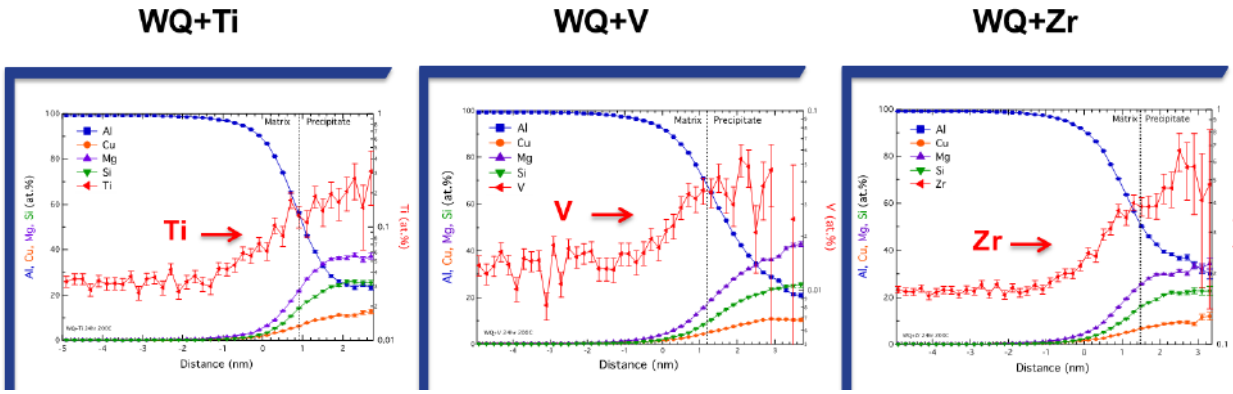

Figure 40. Proxigram results for Ti, V, Zr partitioning into Q-phase but were predicted not to by DFT

4.4 Results from final alloy design

Validating these design concepts and utilizing the experimental results in further calibration of ICME models has enabled refinement of final alloy design involving Q-phase precipitates with better coarsening resistance due to slow-diffusing elemental additions preferentially partitioning to the Q-phase. Table 13 shows the composition of the final prototype alloys. Alloy 1 was optimized for higher Q-phase fraction providing more strengthening than the “Baseline” alloy which was designed earlier. Alloy 2 was a further improvement on the coarsening resistance of Q-phase in Alloy 1 by addition of small amounts of Ni, V and Zr. Extensive mechanical property evaluation of the designed alloy was performed and compared with the target properties as discussed in *Section 2 - Comparison of Developed Cast Alloy properties to DOE Targets.*

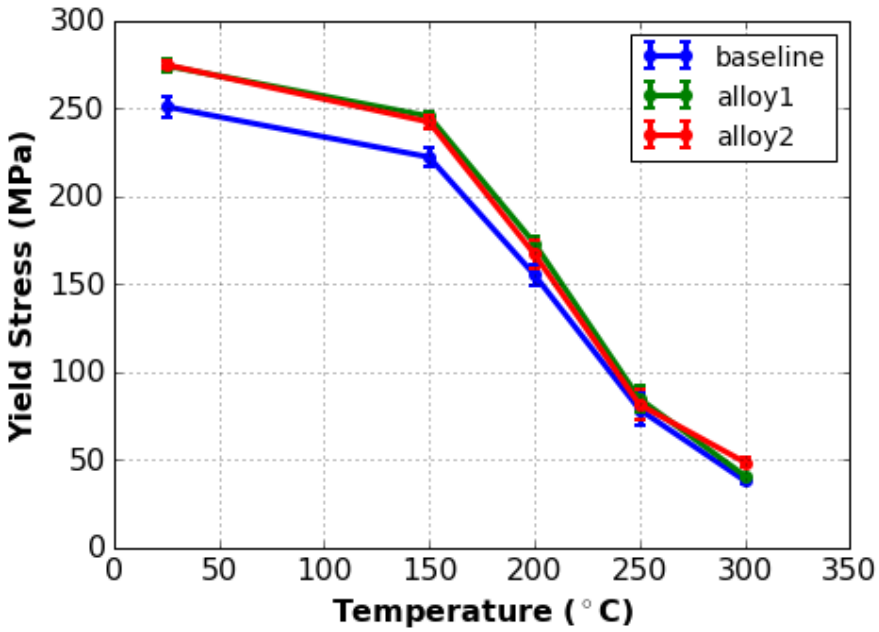

Figure 41. Yield strength result as a function of temperature for 3 different alloys

Figure 41 shows the measured yield strength for each of the prototype alloys. Alloy 2 with the elemental additions showed better strengthening at higher temperature due to a coarsening resistant strengthening precipitate. However, the steep drop in strength at higher temperatures for each of the designed alloys indicated that Q-phase is not necessarily a more effective high temperature strengthener than other precipitates likes θ'-phase or β'-phase, as predicted by coarsening rate constants calculated during the design exercise (refer section 3.1. Design using existing known precipitates).

Table 13. Composition of 3 different prototype alloys

Name	Si	Sr	Ti	B	Mg	Fe	Mn	Cu	Zn	Ca	P	Sn	Ni	V	Zr
Baseline	6.5-7.5	0.005-0.02	0.2	0.05	0.25-0.45	0.2	0.1	0.4-0.6	0.1	0.05	0.05	0.05	0.05	n/a	n/a
Alloy1	7.5-8.5	0.01-0.02	0.1-0.2	0.05	0.35-0.45	0.2	0.15-0.25	0.7-0.8	0.1	0.05	0.05	0.05	0.05	n/a	n/a
Alloy2	7.5-8.5	0.01-0.02	0.1-0.2	0.05	0.35-0.45	0.2	0.15 - 0.25	0.7-0.8	0.1	0.05	0.05	0.05	0.1-0.15	0.1-0.15	0.1-0.15

In order to evaluate the reason behind steep drop in strength, additional TEM study was performed to characterize the Q-phase precipitates at these high temperatures. TEM specimens were prepared from thin-slices (foils) of cut material with dimensions 10 *mm* x 10 *mm* x 0.4 *mm*. These foils were then thinned to 100-200 *μm* in thickness and polished to a 1 *μm* diamond paste polish on both sides. Disks with a thickness of 3 *mm* were punched from the polished foils and then electropolished using a Tenupol 5 machine with a solution of 33% nitric acid and 67% methanol at -15 ˚C to -25 ˚C with an applied voltage of 14 V. To measure the Q-Phase, we exploit the orientation relation of the phase with the Al matrix, taking images in the <110> zone axis of the Al matrix. Images taken down the <110> Al zone axis contains particles 45˚ out of the imaging plane due to the [100] and [010] growth directions of the rod lengths. The measured values for these two directions should be multiplied by a factor of sqrt(2). Results from the TEM work is shown in the figures below (Figure 42).

Loss of orientation relationship is observed at 300˚C, with highly misoriented Q-phase visible in all three samples. Additionally, the Q-phase rods are observed to coarsen significantly in all three alloys at 300˚C. The loss of orientation of the Q-phase rods, in addition to the coarsening of the precipitate is the likely cause for the drastic drop in strength at higher temperatures. This loss of orientation relationship leading to excessive coarsening was not anticipated earlier in the design and would have to be included in any future designs of a Q-phase strengthened alloy for high temperature application.

Utilizing the methods described above, measurements of the length and radius were made and are reported in Table 14. It can be seen from the measurements that Alloy 2 is the most coarsening resistant at all the temperatures, which explains its superior performance. It was also seen that the extent of misorientated Q-phase precipitates was the lowest in the case of Alloy 2.

Table 14. Length and Radius measurement from TEM work

	Baseline		Alloy1		Alloy2	
Temp. (°C)	Length (nm)	Radius (nm)	Length (nm)	Radius (nm)	Length (nm)	Radius (nm)
200	181 ± 54	5.4 ± 1.6	160 ± 38	6.2 ± 2.1	141 ± 51	3.7 ± 1.3
250	333 ± 130	15.8 ± 9.3	389 ± 147	16.0 ± 5.8	358 ± 129	13.3 ± 8.1
300	-	67 ± 23	-	55 ± 16	-	26 ± 11

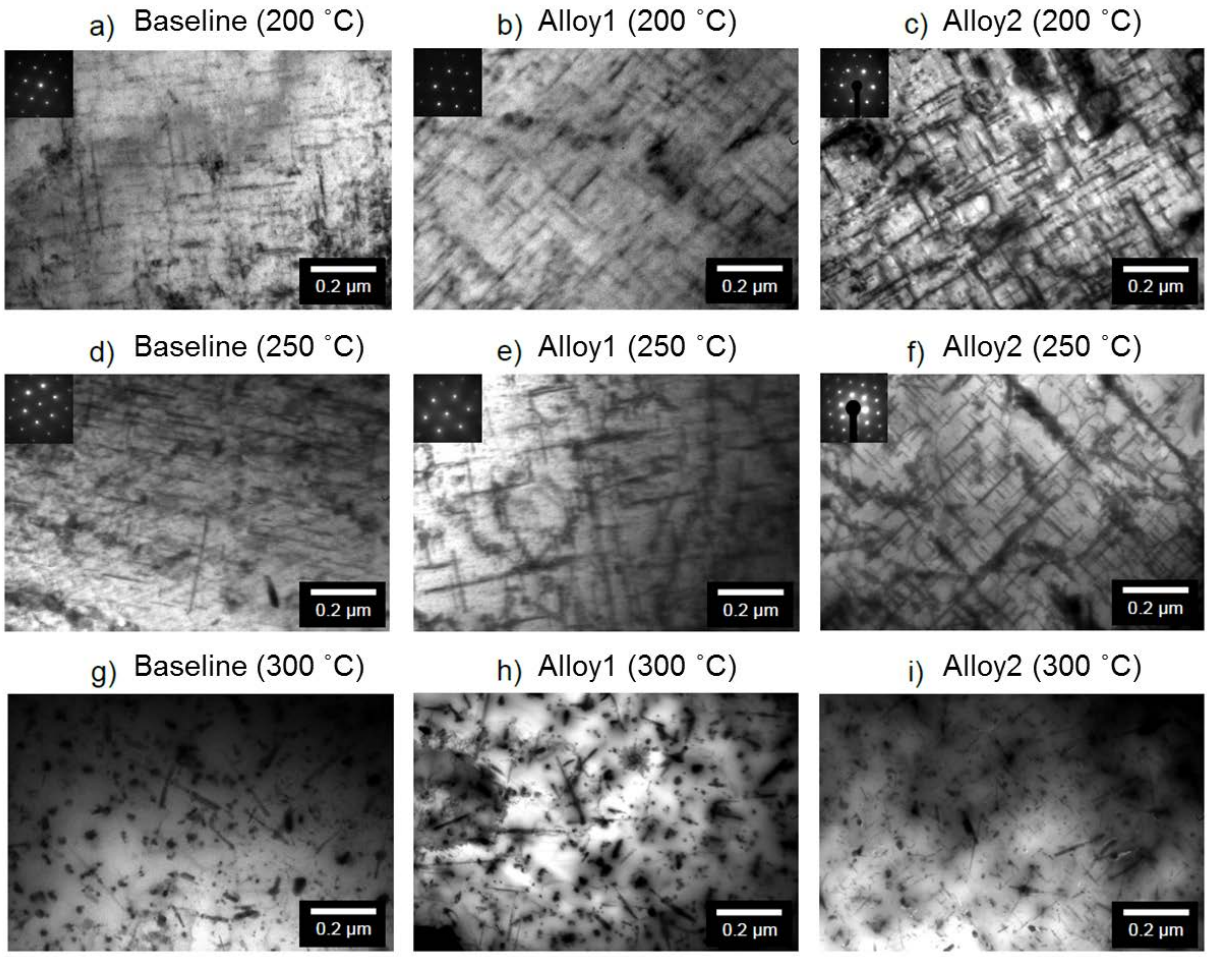

Figure 42. TEM micrographs for the 3 alloy. Images taken along <110> for 200ºC and 250ºC

5. Modeling Approach

5.1 Thermodynamic assessment of Q-phase

An accurate thermodynamic database is required for efficiently designing alloys. The state-of-art thermodynamic database for Q-phase has not being assessed thoroughly and fails to explain the experimental observations, hence requiring updating.

New experimental data for precipitate phase fractions and compositions collected using LEAP analysis were used to update the thermodynamic database for the Al-Si-Mg-Cu system. Data for Q phase composition measured using LEAP indicate a wide solubility range for Cu in Q, ranging from 0-20 at%Cu (Table 15). It was observed that while Al and Si solubility in Q remains fairly constant, Mg solubility varies inversely with Cu, indicating that Cu and Mg might occupy the same lattice site. Updates to the database included incorporating this wide range of Cu solubility, as well as updating the model describing the Q phase. Several models for the Q phase were investigated and the simple model (Al)4(Cu,Mg)3Mg8Si6 was selected based on the present leap results with Cu and Mg in the same sublattice.

Table 15 Experimental (LEAP) and calculated (updated TDB) results for Q phase composition at 200°C

Alloy (at. %)	Al		Cu		Mg		Si	
	Exp.	Cal.	Exp.	Cal.	Exp.	Cal.	Exp.	Cal.
Q2 (Ave.)	18.57	19.05	11.83	12.83	42.49	39.55	27.11	28.57
WQ 72h	21.96	19.05	11.52	11.67	41.18	40.72	25.34	28.57
WTQ 1h	17.94	19.05	20.725	13.14	34.275	39.24	27.06	28.57
WTQ 72h	20.08	19.05	11.77	13.14	40.64	39.24	27.06	28.57
WTQ1 24h	21.07	19.05	12.22	13.14	40.87	39.24	25.83	28.57
WTQ2 3h (no θ?)	22.28	19.05	16.42	13.14	36.04	39.24	25.24	28.57
WTQ2 24h (no θ?)	20.84	19.05	13.65	13.14	37.32	39.24	28.175	28.57
WTQ3 24h (no θ?)	20.02	19.05	13.74	13.05	38.09	39.33	28.13	28.57
CQ 72h	24.06	19.05	10.01	12.57	39.2	39.81	26.72	28.57
CTQ 1h	17.94	19.05	20.12	13.14	35.22	39.24	26.72	28.57
CTQ 72h	No Q	19.05	No Q	13.14	No Q	39.24	No Q	28.57
CM 1h	24.73	19.05	3.47	3.39	39.45	48.99	32.35	28.57
CM 72h	18.34	19.05	5.26	3.39	47.18	48.99	29.2	28.57
Q-Eu 72h	22.77	19.05	9.89	7.67	45.04	44.71	22.29	28.57
356.2 72h	18.03	19.05	0	0	53.11	52.38	28.85	28.57
356.2+Cu 72h	22.1	19.05	11.46	12.61	38.39	39.77	28.06	28.57

The experimental results are compared to the predictions using the database with updated Q-phase model and fcc parameters can be found in Table 15. The Cu lean and rich predicted compositions in Q agree well with experiments. However, the Cu mean compositions remain a little off, but generally by less than 3%. Additionally, predicted phase fractions compared to experimentally observed phase fractions can be observed in Table 16. Updated values for predicted theta phase fraction have decreased due to the modifications to the fcc phase description, resulting in better matching with experimentally observed values.

Table 16 Experimental (LEAP) and calculated (updated TDB) results for phase fractions at 200°C

Alloy (at. %)	Fcc_A1 %		Q_phase %		Al2Cu_Theta %		Si_Diamond %	
	Exp.	Cal.	Exp.	Cal.	Exp.	Cal.	Exp.	Cal.
Q2 (Ave.)	98.39	97.96	1.61	1.77	x	0	x	0.27
WQ 72h	98.72	98.26	1.28	1.63	x	0	x	0.11
WTQ 1h	98.2	95.31	0.92	1	0.89	2.81	x	0.88
WTQ 72h	95.11	95.31	0.9	1	3.1	2.81	0.89	0.88
WTQ1 24h	97.27	96.73	0.64	0.71	2.09	1.78	x	0.78
WTQ2 3h (no θ?)	99.17	97.58	0.83	0.82	x	0.68	x	0.92
WTQ2 24h (no θ?)	99.16	97.58	0.84	0.82	x	0.68	x	0.92
WTQ3 24h (no θ?)	99.12	98.42	0.88	0.87	x	0	x	0.71
CQ 72h	93.47	93.41	1.18	1.25	x	0	5.34	5.34
CTQ 3h	92.83	91.24	0.67(0)	0.77	2.54	3.02	4.93	4.97
CTQ 72h	92.12	91.24	0.66(0)	0.77	3.52	3.02	4.98	4.97
CM 1h	92.83	91.88	0.59	1.26	x	0	6.58	6.86
CM 72h	92.12	91.88	0.94	1.26	x	0	6.95	6.86
Q-Eu 72h	81.57	79.91	5.15	18.26	5.13	1.83	1.6	0
356.2 72h	93.28	93.05	0.58	0.86	x	0	6.13	6.09
356.2+Cu 72h	93.26	92.89	0.94	1.23	x	0	5.8	5.88

The phase boundaries between the Q and Q+θ regions based on the updated database can be found in Figure 43. In addition, experimental data points from prototype alloys are plotted along with the measured Q and θ phase fractions from LEAP. It can be seen that the experimental observations agree with the predicted phase boundaries. Figure 44 shows a comparison between the prediction of phase boundaries using state-of-art Al database from Thermo-Calc (TCAL2) and the new QT modified database. Better agreement to the experimental data is seen from using the QT database. Using the new updated thermodynamic database, new alloy designs were performed to optimize the maximum Q-phase fraction to enhance the precipitation hardening behavior in these alloys.

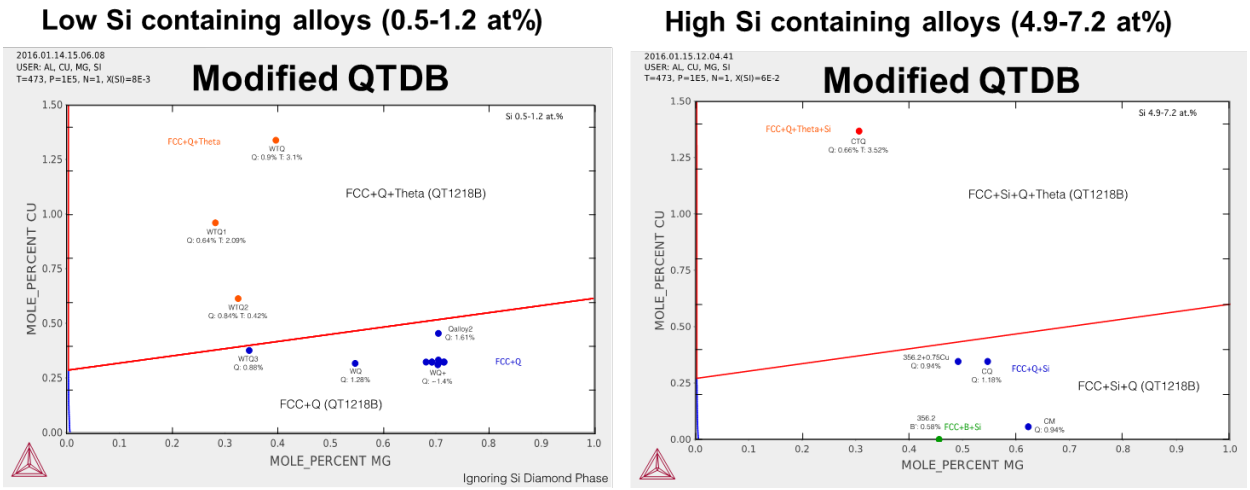

Figure 43 Modified phase boundaries in an isothermal section at 200C with plotted data points indicating experimentally observed phase fractions for (left) wrought alloys and (right) cast alloys. Note: Si phase fraction is ignored in cast alloys.

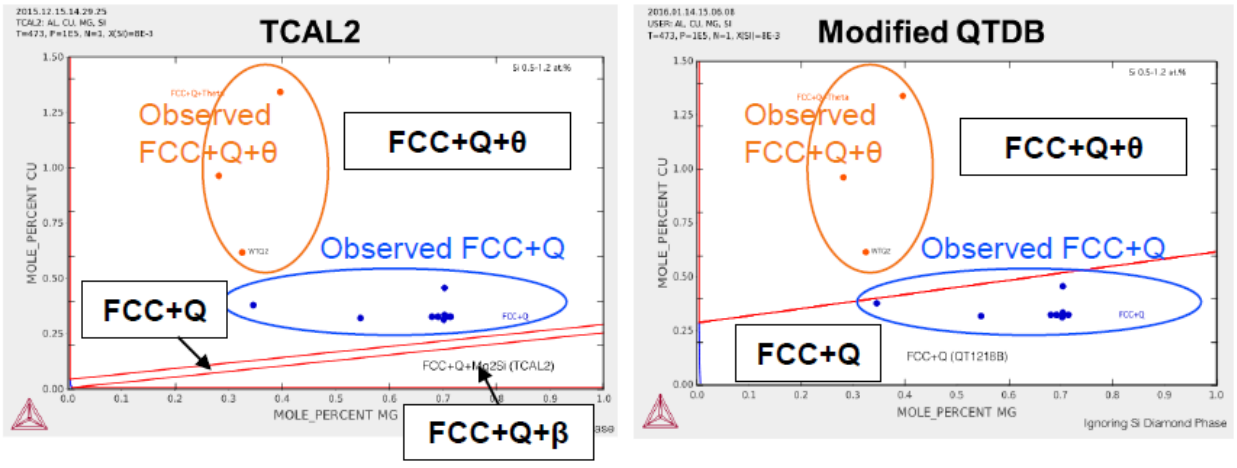

Figure 44. Comparison between TCAL2 and Modified QTAL database. The phase boundaries are compared with experimental results showing improved predictions for QTDB

5.2 Strength Model

Accurate modeling of strengthening mechanisms and precipitate coarsening within high temperature aluminum alloys at elevated temperatures enables the efficient design of engine components to safely operate at these higher temperatures. A modified LSW theory for non-spherical rod-type particles was

developed from both particles measured as part of this work and from those found in literature. Using processing parameters such as alloy composition, aging time, and temperature, the model runs CALPHAD (CALculation of PHAse Diagrams) simulations for additional inputs thereby creating a broad model that is accurate over a wide range of alloy compositions and aging temperatures. In addition, a plate growth model was developed using machine learning for θ'-phase precipitation but is limited by applicable composition and temperature variations due to limited training data.

Three Dimensional Atom Probe Tomography (3DAPT) and Transmission Electron Microscopy (TEM) experiments were performed to measure the particle size and change in composition as a function of aging time for both wrought and cast alloys generated during the project. Accurate rod radii from 3DAPT and particle lengths from TEM were used to determine the effects of aging temperature and time on particle coarsening. The Lee coarsening model [3] was adapted for use in describing the evolution of the Q-phase rod particles as both a function of aging time and temperature. Experimental measurements and an extensive curation of archival literature data were used to calibrate the Lee model and is shown to describe the particle evolution well (see Figure 45). The development of a coarsening model for θ'-phase platelets was performed using machine learning (ML). Using experimental particle size measurements and data from the literature as input, the ML code was found to describe the plate thickness and diameters well within the bounds of the training data.

An age hardening model was developed to describe the evolution of the yield strength as a function of aging time, aging temperature, and test temperature for aluminum alloys with rod and plate-type precipitates. The Orowan equation was modified for finite rods oriented down $\langle 100 \rangle_{\alpha\text{-Al}}$ as a function of both radius and length. Orowan strengthening was expanded to include test temperature dependence through incorporation of the previously discussed rod and plate-type particle growth models and a temperature dependent matrix shear modulus. Evolution of the volume fraction of the Q- and θ'-phases with respect to aging temperature and time is included using the Shercliff process model [6]. Only the dislocation bypass mechanism was considered for the rod and plate-type particles. In addition to precipitation strengthening the developed strengthening model includes temperature dependence for base aluminum yield strength, SSS, and Si eutectic strength enhancements. The SSS was incorporated for Mg, Si, and Cu additions to the aluminum system using the Feltham trough model [7-13]. The trough model was calibrated for the Al-Mg binary system and traditional scaling factors were considered for Cu and Si contributions, while the Si eutectic contribution was estimated using a rule of mixture (ROM) Reuss model for the Young's modulus [14], where the temperature dependence was incorporated in the Young's moduli of the matrix and Si phases. The model has no variable calibration terms between different alloy systems and uses CALPHAD calculated phase equilibria and process variables as input parameters.

The developed strengthening model was found to agree well with experiment particularly at long aging times and high-temperatures. Figure 47(a) compares the measured tensile strength versus the predicted high-temperature yield strength from the model for six different alloys: 356, AS7GU and Ct-0.8Cu from the Part 1 companion report, Ct-3.2Cu, Ct-0.8Cu-v2, and Wt-0.8Cu. The mean average error MAE for these HT alloys is 18.6 MPa and a PCC of 0.97 between the experiment and model predictions. There is an extremely good correlation between the strength model and the elevated temperature tensile experiments. Figure 47(b) shows the temperature dependence on the yield strength for four of the alloys: Ct-3.2Cu, Wt-0.8Cu, Ct-0.8Cu-v2, and 356. The yield strength model shows excellent agreement with the yield strength data over all aging and testing temperatures for the Q-phase and θ'-phase strengthened alloys. The model captures the trend of decreasing strength with temperature very precisely with similar drops in strength between each tempering condition. The yield strength model also correctly captures the correct ordering of the various alloys strengths, with the Ct-3.2Cu alloy having the greatest RT strength, followed by alloys

Wt-0.8Cu and Ct-0.8Cu-v2. The model is seen to slightly overpredict the strength of the Ct-3.2Cu alloy and is due to an overestimation of the θ' phase fraction from the database. Like the experimental data, the predicted yield strengths converge at high testing temperatures; however, for Ct-3.2Cu and Ct-0.8Cu-v2 the model slightly over predicts the strength at 300°C. It is important to note that the β strengthened 356 alloy is lower in YS over all aging temperatures than the Q-phase strengthened alloys, demonstrating the benefit of Q-phase strengthening for high-temperature applications. Figure 47(c) shows the individual contributions from: precipitation strengthening, SSS, and intrinsic strength for the Ct-0.8Cu-v2 alloy. The total alloy strength is dominated by the Orowan strengthening contribution and leads to the distinctive drop in strength with temperature. The SSS strength contribution is small due to the small amount of solubility in the matrix after precipitation, but is found to have a minimum which occurs due to the dissolution of the Q-phase at higher aging temperatures thereby introducing more solute back into the matrix. The intrinsic strength is very low and decreases slightly with temperature. The yield strength model is found to accurately predict strength at all aging temperatures and over a wide range of Al-Si-Mg-Cu alloy compositions. The model limitations with respect to β-phase strengthened alloys like 356 due in part to the morphological change that occurs upon aging.

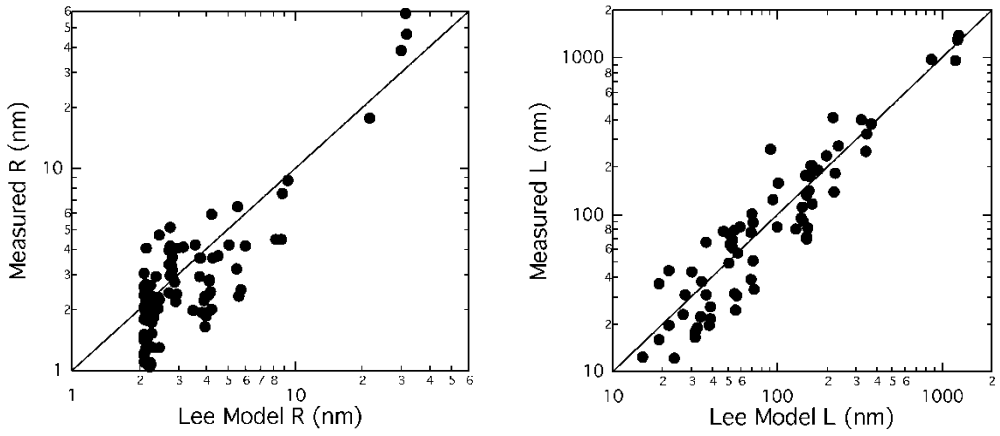

Figure 45 Measured vs predicted (a) radius and (b) length for the modified Lee model.

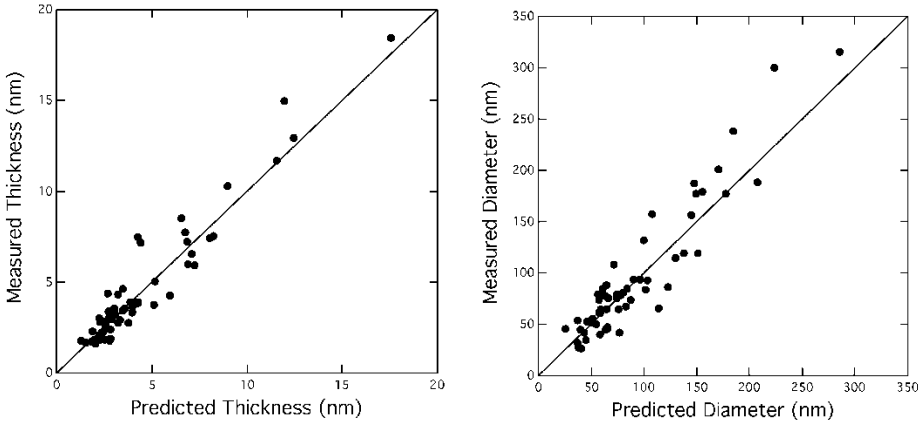

Figure 46 Measured vs predicted (a) thickness and (b) diameter for the ML model.

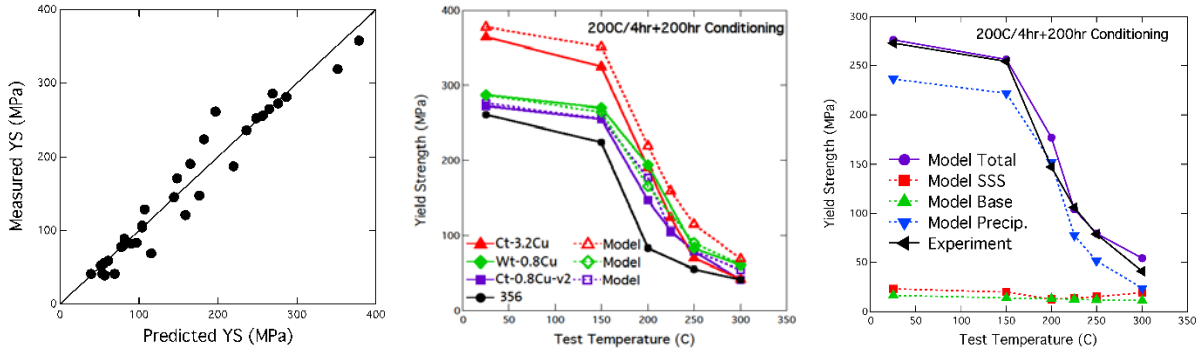

Figure 47 (a) Comparison between experiment and predicted yield strength for the high-temperature tensile tests. (b) Tensile yield strength for alloys Ct-3.2Cu, Wt-0.8Cu, Ct-0.8Cu-v2, and 356 for testing temperatures ranging from RT to 300°C. (c) Individual strengthening contributions for the Ct-0.8Cu-v2 alloy as a function of temperature.

After calibration of the strength model to capture precipitation strengthening, solid solution strengthening, and temperature effects as described in the previous section, the calibrated strength model was applied and compared to measured strength data for casting trial Alloys 1 and 2 (compositions given in Table 13). Table 14 provides the measured lengths and radii of Q-Phase precipitate in different alloys as a function of temperature after 100h of aging. Utilizing the strength model developed previously, estimates of the yield strength was made for each of the case. The strength model accounted for the uncertainty in the measurements of length and radius providing a range of predicted strength in each case. Figure 48 shows the results from this exercise. The band of each color shows the bounds of the prediction over the experimental uncertainty involved in the measurements of radius and length.

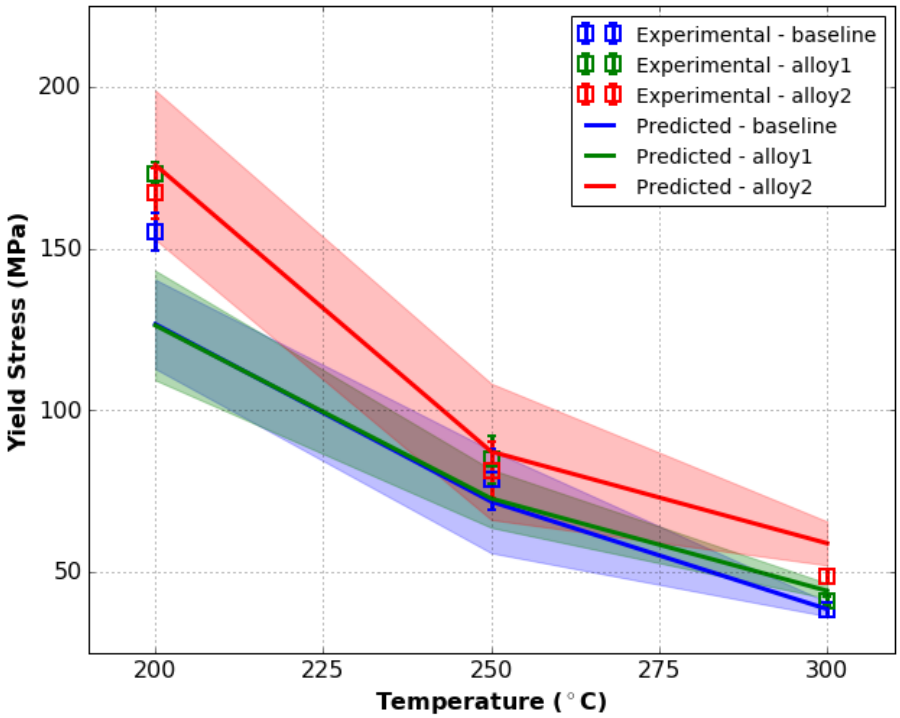

Figure 48. Comparison of the experimental yield strength with the predicted strength (uncertainty bounds given by shaded regions).

The following inferences can be drawn from the model predictions:

1. The model seems to under-predict the strength at 200˚C for baseline and Alloy 1. The predicted strength of Alloy 2 seems to agree well with the experimental results. The reason for under-prediction in the other two cases can be attributed to the excessive coarsening of the precipitates seen in the TEM experiments. Further evaluations are warranted to understand this anomaly.
2. Experimental 250˚C strength lies within the prediction bands for the alloys explaining the observations. The strength of Alloy 1 is slightly under-predicted. Reasons for this cannot be explained by the model.
3. The model is over-predicting the strength for Alloy 2 at 300˚C which could possibly be due to not including the effect of precipitate misorientation in reducing the strengthening effect due to precipitate hardening.

The strength model was able to capture the trends correctly but did not show good agreement with experimental values. Further modifications to the strength model are suggested for improvements:

1. Varying the pre-factor for Orowan strengthening contribution calculations to increase the strength of Alloy 1 and baseline at 200°C. This will lead to overestimation of yield strength for the other cases, for example as shown in Figure 49. Careful recalibration needs to be performed to account for both underestimation and overestimation.

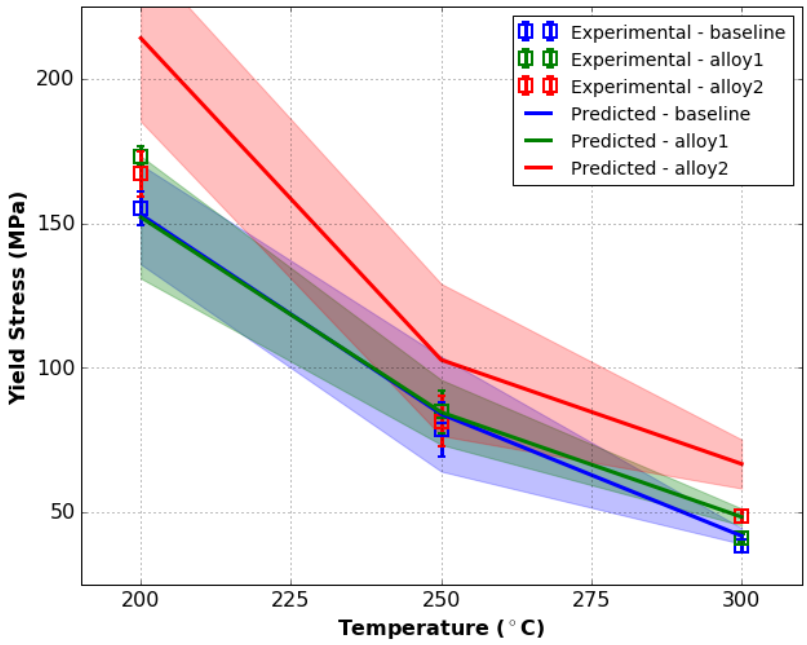

Figure 49. Effect of changing Orowan equation prefactor on predicted strength

2. Investigate if the addition of minor elements is leading to a different microstructural change that is not captured in the model currently (e.g. Hall-Petch effect).
3. Include the effect of loss of orientation relationship on the precipitation strengthening effect.

6. Design Issues and Gaps

Previous sections have outlined the design approach, tools and results from the alloy design exercise during the program. Utilization of ICME tools have helped considerably in accelerating the design process but several gaps and design issues were met during the course of the program which were not previously anticipated. The following section will attempt to elucidate some of these issues and gaps for future implementation of ICME tools and methods in design of alloys.

6.1 Use of RT strength/ Hardness as a proxy for high temperature strength

Different alloy design concepts were evaluated using Vickers Hardness testing at room temperature after appropriate aging treatment. It was assumed that a higher room temperature strength would translate into a higher high temperature strength but to the contrary, it was observed that higher room temperature strength alloys suffered with steeper drop in strength at high temperatures resulting in near equal strength at these temperatures. Figure 33 explains this phenomenon seen in the tensile test results of different Castalloy designs tested at multiple temperatures. CastalloyTQ exhibited the highest room temperature hardness in the experiments and was assumed to have the same superior strength at higher temperature, however at 300 ˚C CastalloyQ had higher strength than CastalloyTQ.

6.2 Misalignment and excessive coarsening of Q-phase at high temperature

Initial calculations for coarsening rate constants showed better coarsening behavior for Q-phase as compared to θ'-phase making it a promising candidate precipitate for strengthening Al-alloys and achieving good high temperature strength. However, TEM observations of alloys at higher temperature and longer times showed the presence of large misaligned Q-phase precipitates. Initial results at 200°C were very

promising in terms of Q phase stability and strength. However, observed misalignment effects at 250 and 300°C were not taken into consideration in the design concepts due to lack of experimental evidence of this effect prior to the current project.

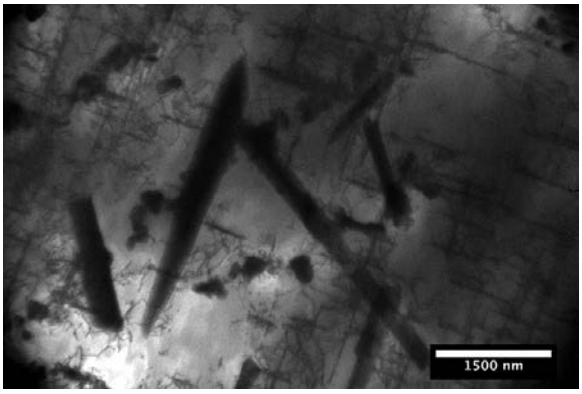

Figure 50 TEM micrograph of a 356 0.75%Cu alloy 300°C/200hr tilted down the <110> direction. Small aligned Q-phase rod shaped particles and large misaligned rods are both visible.

A few postulations about the origin of these misorientated Q-phase particles at higher aging temperature and at longer times are described here:

1. Dissolution of oriented rod particles to re-precipitate Q-Phase at multiple orientation relationships appearing as randomly misoriented particles. This explanation could not explain why a spontaneous dissolution of the finer particles would occur in the first place and also the reason for such rapid coarsening of the newly precipitated particle.
2. Spheroidization of Q-Phase similar to spheroidization of cementite[1] observed in steels which is due to a balance of misfit strain energy and interfacial energy. Currently this explanation holds the highest promise and can be modeled by replicating similar models developed for cementite and for "ovulation" of MnS. Experimental evidence for spheroidization will help in confirming the theory and also validating the model.

7. Recyclability Analysis

GM collaborated with American Foundry Society and SECAT to evaluate the recyclability of the alloy developed for high temperature lightweight cast alloy for advanced cylinder heads in high-efficiency, light-duty engines. Because the chemistry of the final alloy is confidential, a set of five alloys were developed for analysis and compared to a baseline A356.1 material. These five alloys encompass the selection of elements combinations that would be used in the final alloy. Each of the elements are evaluated on the potential impact on the recyclability of the material. Furthermore the list of five alloys progresses from the baseline A356.1 alloy to A356.1+0.5 Cu to A356.1+0.5 Cu with each of the added minor elements. In this manner, an evaluation of the added cost of each of the elements can be obtained as well as the increased cost of the total alloy. The alloy costs are then used in the cost models developed for the semi-permanent mold casting process used for cylinder head production. The impact of copper and the minor elements on the recyclability stream was proven to be negligible. Because of the very large cycling stream for aluminum, these minor elements will be essentially diluted to negligible amounts. Also as these elements are contained

[1] Luzginova, N. V., L. Zhao, and J. Sietsma. "The cementite spheroidization process in high-carbon steels with different chromium contents." *Metallurgical and Materials Transactions A* 39, no. 3 (2008): 513-521.

in other wrought or cast aluminum alloys, these elements are not seen as detrimental to the aluminum recyclability market. Full details of the recyclability analysis were provided in previously submitted milestone reports.

8. Cost Analysis

GM subcontracted Camanoe Associates to develop a comprehensive cost model covering alloy production, capital costs, processing methods, and component finishing costs for annual production runs up to 500,000 units, in increments of 100,000 units. The cost models made a direct comparison of capital alloy production, processing, and component finishing costs with baseline component costs sufficient to complete evaluation of the cost effectiveness of the new material. The set of five alloys use in the recyclability analysis were also used in this cost analysis. Only for the fifth alloy composition did the overall costs exceed 110% of the baseline alloy process costs. Full details of the cost analysis were provided in previously submitted milestone reports.

9. Technology Requirements

In order for a new alloy to go into production the following requirements need to be met:

- Mechanical properties including tensile and fatigue properties up to 300 ^{o}C extracted from cylinder head castings for planned production part.
- Physical properties including density, thermal conductivity, fraction solid curves, specific heat, latent heat, viscosity, and surface tension for fill and casting defect simulations. Thermal expansion coefficients.
- Casting simulation analysis of new alloy for planned production head casting
- Cost analysis for component level piece cost and tooling costs.
- Casting quality: X-ray, visual, and leak test evaluation of castings.
- Hydraulic and steam thermal fatigue tests.
- Engine Test simulation analysis.
- Global Engine Thermal Cycle (GETC) and Global Engine Durability (GED) tests.

A new alloy must sufficiently exceed the benefits of a current production alloy in meeting these tests to justify their implementation into the Bill of Materials and Bill of Process for production of head castings.

10. Products Developed Under the Award

10.1 Publications

1. First-principles/Phase-field modeling of θ' precipitation in Al-Cu alloys, Acta Materialia 140 344-354 (2017)

2. Equilibrium composition variation of Q-phase precipitates in aluminum alloys, Acta Materialia (2017)

3. First-principles study of crystal structure and stability of T1 precipitates in Al-Li-Cu alloys, Acta Materialia 145 337-346 (2018)

4. Ostwald ripening of spheroidal particles in multicomponent alloys, Acta Materialia 152 327-337 (2018)

5. Energetics of native defects, solute partitioning, and interfacial energy of Q precipitate in Al-Cu-Mg-Si alloys, Acta Materialia 154 207-219 (2018)

6. Enhanced Coarsening Resistance of Q-phase in Aluminum alloys by the addition of Slow Diffusing Solutes, Materials Science & Engineering A 735 318-323 (2018)

7. Interfacial stability of θ'/Al in Al-Cu alloys, Scripta Materialia 159 99-103 (2019)

8. High Temperature Aging of Al-Si-Mg Alloys: Part 1-CALPHAD Precipitation Growth Model Pending Publication

9. High Temperature Aging of Al-Si-Mg Alloys: Part 2 CALPHAD Precipitation Strengthening Model Pending Publication

10. Progress and Gaps in Thermodynamic Modeling for the Development of Advanced Cast Aluminum Alloys using Integrated Computational Materials Engineering, Presented at TMS 2017 Annual Meeting and Exhibition February 2017

10.2 Patents

Stabilized Aluminum Casting for Elevated Temperature Applications, Patent Application 15/153402 dated 12/May/2016, Published Application 2107-0327929-81 dated 16/Nov/2017

A Method to Increase the amount of Zr in Solid Solution in Aluminum alloys by the insertion and dissolution of Cu-Zr alloys and powders, Patent Application 15/481666 dated 07/Apr/2017

A Method to Increase the Room and High Temperature strength of Aluminum by the Addition of TiCu Compound in the Melt, Patent Application 15/975159 dated 9/May/2018

11. References

[1] Clyne, T.W. and Davies, G.J.: Br. Foundryman, 1981, vol. 74, pp. 65-73.

[2] Yan, X. and Lin J.C., Metall Mater. Trans., vol. 37B, pp. 913-918 (Dec 2006).

[3] I. M. Lifshitz and V. V. Slyozov, "The Kinetics of Precipitation from Supersaturated Solid Solutions," *J. Phys. Chem. Solids*, vol. 19, pp. 35–50, 1961.

[4] C. Wagner, "Theorie der Alterung von Niederschlägen durch Umlösen," *Zeitschrift für Elektrochemie*, vol. 65, pp. 581–591, 1961.

[5] H. C. Lee, S. M. Allen, and M. Grujicic, "Coarsening resistance of M2C carbides in secondary hardening steels: Part I. theoretical model for multicomponent coarsening kinetics," *Metall. Trans. A*, vol. 22A, pp. 2863–2868, 1991.

[6] H. R. Shercliff and M. F. Ashby, “A process model for age hardening of aluminum alloys- I. The model,” *Acta Mater.*, vol. 38, pp. 1789–1802, 1990.

[7] P. Feltham, “Solid solution hardening of metal crystals,” Br. J. Appl. Phys., vol. 1, pp. 303–308, 1968.

[8] M. Z. Butt, K. M. Chaudhary, and P. Feltham, “Plastic flow in BCC solid solutions,” J. Mater. Sci., vol. 18, pp. 840–846, 1983.

[9] M. Z. Butt, P. Feltham, and I. M. Ghauri, “On the temperature dependence of the flow stress of metals and solid solutions,” J. Mater. Sci., vol. 21, pp. 2664–2666, 1986.

[10] M. Z. Butt. 1988, “Correlation between temperature dependence of critical resolved shear stress and nature of solute distribution in aluminium-magnesium alloys,” J. Mater. Sci. Lett., vol. 7, pp. 879–880, 1988.

[11] P. Feltham and N. Kauser, “Solid-Solution Hardening,” Phys. Status Solidi A, vol. 117, pp. 135–140, 1990.

[12] M. Z. Butt, “Stress equivalence of solid-solution hardening,” J. Phys. Condens. Matter, vol. 2, pp. 5797–5808, 1990.

[13] M. Z. Butt and P. Feltham, “Review Solid-solution hardening,” J. Mater. Sci., vol. 28, pp. 2557–2576, 1993.

[14] F. Lasagni and H. P. Degischer, “Enhanced Young’s Modulus of Al-Si Alloys and Reinforced Matrices by Co-continuous Structures,” J. Compos. Mater., vol. 44, pp. 739–755, 2010.

12. Acknowledgement and Disclaimer

Acknowledgment: This material is based upon work supported by the Department of Energy under Award Number(s) DE-EE0006082.